

**AEROSOL OPTICAL PROPERTIES IN SEOUL MEASURED USING THE
UW-MADISON HSRL**

by

Coda Phillips

A thesis submitted in partial fulfillment of
the requirements for the degree of

Master of Science

(Atmospheric and Oceanic Sciences)

at the

UNIVERSITY OF WISCONSIN-MADISON

2019

The thesis is approved by the following members of the Final Committee:

Steve Ackerman, Professor, AOS

Grant Petty, Professor, AOS

Tristan L'Ecuyer, Professor, AOS

ACKNOWLEDGMENTS

I would like to acknowledge and thank Robert Holz, Ralph Kuehn, and Willem Marais, my mentors throughout my graduate work. My thanks also go to Ilya Razenkov and Ed Eloranta for helping me with technical lidar issues.

Also, this thesis was composed with data graciously provided by Xian Peng and Sang-Woo Kim.

Finally, I'd like to thank those who read and commented on the thesis: Steve Ackerman, Grant Petty, and Tristan L'Ecuyer.

CONTENTS

Contents ii

List of Tables iv

List of Figures v

1 Review 1

1.1 *Introduction* 1

1.2 *Overview of Aerosol in East Asia* 1

Aerosol Climatology of South Korea	2
Anthropogenic Particulate Matter	3
Dust	3
Biomass Burning	4
Aerosol Optical Depth	4
Surface Particulate Matter	4
Diurnal Cycle	5
Air Quality Trends	5

1.3 *Overview of Aerosol Observations* 6

Passive aerosol remote-sensing	6
Lidar aerosol observation	7
In-situ observation	7
Common Limitations	8
KORUS-AQ	8

2 Methods 10

HSRL Theory	10
HSRL Calibration Challenges	13
Aerosol Extinction vs. Aerosol Backscatter Coefficient	13
Aerosol Lidar ratio	14

HSRL measurements of the Lidar Ratio	15
HSRL sensitivity to aerosol	16
Aerosol Modeling	17
AERONET	18
University of Wisconsin HSRL	18
HSRL molecular extinction	19
HSRL-based AOD	19
Manual HSRL Cloud Masking	20
Separating dust from smoke/pollution using linear depolarization .	23
3 Results and Discussion 25	
Lidar Ratio	25
Seasonal Cycle	27
Diurnal Cycle	30
Weekly cycle	32
Dust and polarization	34
3.1 <i>Vertical Profiles of Backscatter</i> 36	
Seasonal Profiles	37
Dust and Polarization	39
3.2 <i>Vertical Profile of Lidar Ratio</i> 43	
3.3 <i>Surface</i> 44	
Correlation with Backscatter	44
Column aerosol mass	48
Dust and Polarization	51
4 Conclusion 55	
References 57	

LIST OF TABLES

2.1 Description of symbols	12
--------------------------------------	----

LIST OF FIGURES

2.1	Two methods of estimating column AOD are validated using AERONET as ground-truth. The first method in blue (Mol. AOD) uses the geometrically-corrected HSRL molecular signal to determine optical depth and is independent of AERONET. The second method in orange (S_a AOD) is computed by integrating aerosol backscatter and fitting a lidar ratio to AERONET for each month and linearly interpolating these to the actual time resolution. This figure shows the low-AOD range and the Fig. 2.2 shows the high-AOD range. Median absolute difference (MAD), including data for larger AOD, is shown in the legend as a performance metric.	21
2.2	Similar to Fig. 2.1, but scale shows high-AOD range.	22
2.3	An example day of cloud-masking HSRL data with altitude on the y-axis and time on the x-axis. The image is an RGB combination of aerosol backscatter coefficient, aerosol depolarization ratio, and color ratio. Water clouds and precipitation are colored orange and ice clouds are green. In this example, automated cloud-masking misses the precipitation and cloud edges. The color band near the surface is caused by the limitations of the near-surface 1064 nm channel.	23
3.1	Time-series of monthly bulk lidar ratio. The bulk lidar ratio is computed using both the AERONET and HSRL-derived AOD (the numerator). In dark blue is the AERONET-based mean and a fill indicating 1 standard deviation. In light blue is the mean based on the geometrically-corrected HSRL molecular signal, which includes a both day and night retrievals compared to the day-only AERONET. For comparison, two average relative humidities from ERA5 are also plotted. One is a simple column average, the other is vertically-weighted by HSRL aerosol backscatter. .	26

3.2	The AERONET-based lidar ratio and backscatter-weighted relative humidity averaged every 20min are plotted for each season. A linear fit was computed for each season and for the entire year. The monthly-mean values are also plotted in red.	27
3.3	Various estimates of monthly-median aerosol optical depth (AOD) in Seoul. Top: All data sampled as AERONET and the effect of lidar ratio is demonstrated by comparing the constant lidar ratio assumption (blue) and interpolated mean lidar ratio (green). Bottom: AERONET AOD and HSRL estimates of AOD. "Cloudless" is defined as having no clouds or virga below the top of integration at 10km. "Cloudless 5km" only integrates to 5km and includes scenes with clouds between 5km and 10km. "Mol. AOD" is the molecular-derived AOD and is sampled the same as "cloudless". All HSRL estimates except "Mol. AOD" assume a bulk lidar ratio interpolated from AERONET-derived monthly means.	29
3.4	AERONET and HSRL AOD estimates aggregated by season and hour-of-day. Descriptions of HSRL various estimates are given in Fig. 3.3. Aggregation excludes hours without adequate representation in each month of the season to prevent some leakage from seasonal AOD trends when sunrise and sunset times co-vary. The seasonal-mean (all inclusive) is plotted as a dotted horizontal line.	31
3.5	Diurnal deviation of AERONET and HSRL AOD estimates aggregated by season and hour-of-day. Similar to Fig 3.4. but daily mean is subtracted.	32
3.6	Daily mean deviation from weekly mean grouped by day-of-week. Integrated aerosol backscatter coefficient is used for all but one (Molecular AOD) of the HSRL estimates. Interquartile range (IQR) is also plotted to show variance.	33
3.7	Time-series of coarse-mode and dust column optical properties. The black line is monthly-median AERONET coarse-mode AOD. The green line is monthly-median matched dust backscatter integrated up to 10 km. Interquartile range (IQR) is plotted to show variance.	35

3.8	Seasonal comparison of coarse-mode AOD and integrated dust backscatter coefficient. Blue dots represent individual matchups between AERONET and HSRL. Red dots show the monthly means for each season. The slope (m) and coefficient of determination (r^2) from linear regression are shown in the legend.	36
3.9	Time-series of decomposed bulk lidar ratio. The black line repeats the monthly bulk lidar ratio from Fig. 3.1 (using median instead of mean has little effect). The green line shows the dust bulk lidar ratio (defined as coarse-mode AERONET AOD divided by integrated HSRL dust backscatter). The blue line shows the non-dust bulk lidar ratio (defined as fine-mode AERONET AOD divided by integrated HSRL non-dust backscatter).	37
3.10	Vertical profile of aerosol backscatter coefficient below 4km. The median value and inter-quartile range (IQR) for each season is displayed. . . .	38
3.11	Vertical profile of aerosol backscatter coefficient between 4km and 10km. Similar to Fig. 3.10 but at higher altitude and smaller y-scale.	39
3.12	Seasonal-mean vertical profiles of dust and non-dust backscatter coefficient and dust fraction at 7.5m vertical resolution. The dashed black line shows seasonal-mean non-dust backscatter coefficient (ν_{nd}). The solid black line has been corrected for hygroscopic growth. The blue line shows dust backscatter coefficient (ν_d). The dashed green line shows the ratio of median dust to median aerosol backscatter coefficient ($\frac{\nu_d}{\nu_{nd} + \nu_d}$). The solid green line is the same ratio, but using the corrected non-dust backscatter coefficient (dashed black line).	41
3.13	Seasonal-mean vertical profiles of dust and non-dust mass concentration from NAAPS aerosol model. The black line shows the non-dust mass concentration. The blue line shows dust mass concentration. The dashed gray line shows the median dust fraction of median total mass concentration.	42

- 3.14 Vertical profile of median lidar ratio. In orange, KORUS-AQ data from airborne NASA HSRL2 included for comparison. The UW-Madison HSRL mean for the entire year is shown in dashed blue. The UW-Madison HSRL mean from the same time period as the NASA HSRL2 is also displayed as a solid blue line. The minimum, maximum, and mean monthly-mean bulk lidar ratio (time-series in Fig. 3.1) is also plotted as a black line and filled interval. 45
- 3.15 Seasonal comparison of near-surface aerosol backscatter coefficient and $PM_{2.5}$. Blue dots are matchups between hourly $PM_{2.5}$ and the backscatter observation that is nearest in time. Red dots are monthly averages of $PM_{2.5}$ and backscatter. Linear regression results (line slope and coefficient of determination) are displayed in legend. 46
- 3.16 Seasonal comparison of surface relative-humidity (RH) and ratio of non-dust backscatter coefficient to $PM_{2.5}$. Blue dots represent matchups between hourly $PM_{2.5}$ observations and the HSRL backscatter nearest in time. Seasonal means binned by RH are computed and displayed in red. The annual mean binned by RH is repeated in each season as a solid black line. The ratio of 85% and 45% is computed and shown in legend and horizontal dashed black lines highlight the values used. Estimated extinction ratio ($\sigma_{s,nd}/PM_{2.5}$) is displayed in orange to show that the probable dependence of lidar ratio on relative humidity would strengthen the effect. 47
- 3.17 Seasonal comparison of HSRL-estimated $PM_{2.5}$ and observed $PM_{2.5}$. Blue dots represent matchups between hourly observed $PM_{2.5}$ and HSRL backscatter nearest in time. Red dots show the monthly mean in each season. The median absolute error (MAE) is computed and displayed in the legend of each season. 49

3.18	Time-series of median column dry fine-mode mass (integrated $PM_{2.5}$). The green line is NAAPS aerosol model fine-mode integrated mass concentration which outputs at 6-hour time resolution. The blue line is the HSRL-derived column fine-mode mass up to 10km from the cloudless subset. The purple line is the HSRL-derived column fine-mode mass (up to 5km) from the "cloudless 5km" subset. Interquartile range (IQR) is plotted to show variance. Derivation of mass is detailed in methods. The median HSRL-derived AOD from "cloudless" subset is plotted as a dashed line for comparison.	50
3.19	Seasonal comparison of near-surface aerosol backscatter coefficient dust fraction and surface relative humidity. Blue dots show hourly relative humidity from ERA5 and the matched HSRL aerosol backscatter coefficient dust fraction nearest in time. Both are sampled near the surface. Coefficient of determination (r^2) from linear regression is shown in the legend.	52
3.20	Seasonal comparison of near-surface non-dust backscatter coefficient and surface relative humidity. Figure details similar to Fig. 3.19.	53
3.21	Seasonal comparison of near-surface dust backscatter coefficient and surface relative humidity. Figure details similar to Fig. 3.19.	54

AEROSOL OPTICAL PROPERTIES IN SEOUL MEASURED USING THE UW-MADISON HSRL

Coda Phillips

Under the supervision of Professor Steve Ackerman
At the University of Wisconsin-Madison

The University of Wisconsin High Spectral Resolution Lidar (HSRL) was operated continuously at Seoul National University as part of the Korea-United States Air Quality Study (KORUS-AQ). Using the UW-Madison HSRL, AOD can be derived at any time of day and with great frequency. Direct daytime comparisons of the HSRL-derived and AERONET-derived AOD show good agreement. However, the HSRL makes a much larger volume of measurements available. These measurements show qualitative differences from AERONET in the mean diurnal cycle for some seasons. Furthermore, AOD tendency at night can also be characterized. The HSRL is also able to separate dust and non-dust using signal depolarization, average dust and non-dust backscatter is highest near the surface and decreases with increasing altitude. Meanwhile, the fraction of backscatter attributable to dust is small near the surface and increases to about 50% in the free troposphere. Finally, surface $PM_{2.5}$ and near-surface backscatter were found to be highly correlated and the ratio was dependent on relative humidity.

1 REVIEW

1.1 Introduction

In the past decade, coincident with rapid industrialization and economic growth, East Asia has experienced a problematic decline in regional air quality (Chan and Yao, 2008). The effects on health such as cardiovascular disease and lung cancer have been documented and are responsible for approximately 1.9 million deaths per year in the Western Pacific and South East Asia (WHO, 2016). The geographical focus of this thesis is Seoul, South Korea. About half of all Koreans live in the Seoul Metropolitan Area (SMA) (UNdata, 2019). In response to a history of high particulate levels in SMA, multiple clean air acts have been passed, and from those regulations, significant progress towards air quality goals was achieved (Kim and Lee, 2018; Kim et al., 2017c). Still, understanding the sources and causes of poor air quality in Seoul has the potential to improve policies and future public health.

This thesis presents and analyzes long-term lidar measurements from the UW-Madison HSRL located in Seoul during the KORUS-AQ field campaign. The first focus is on documenting and explaining the seasonal, diurnal, and vertical tendencies of aerosol optical properties, including optical depth, lidar ratio, and depolarization. Another focus is on developing dust decomposition, mass estimation, and other methods from which future long-term HSRL studies can build.

1.2 Overview of Aerosol in East Asia

The study of aerosols and air quality in East Asia has received a great deal of attention in the past decade from a variety of groups. Some examples of aerosol-oriented field campaigns conducted in the region are the following: ACE-Asia, APARE, TRACE-P, PEM-WEST, EAREX, APEX, PEACE, CAREBeijing, MAPS, and KORUS-AQ. These field experiments collected intensive observations and established long-running observational capabilities that formed much of our current understanding of the region. The aerosol climatology of East Asia has been rela-

tively well established, as well as the primary factors driving the climatological mean. It's important to review the present state of our understanding of the aerosol climatology in Korea, so the UW-Madison HSRL results can be presented in context and better interpreted.

Aerosol Climatology of South Korea

First, understanding the meteorological climate is critical to understanding the aerosol climate as they are closely correlated. The transport of either dust or pollution depends on the wind. In the absence of transport, meteorological factors also influence the local response of the aerosol environment to local emissions. The meteorological climate of Seoul is classified as Koppen humid continental with dry winter (Peel et al., 2007). It is located in a frontal regime, and the polar jet will often pass overhead during the year. Mid-latitude cyclones as well as typhoons often impact the Korean peninsula.

The East Asian monsoon exerts the most significant control over the intra-annual variability in the region's meteorology. In the winter, the northeastern monsoon winds bring cold Siberian air south into the East Asian region. When spring arrives, lows that form in the west cause outbreaks of dust, known as HwangSa. This is also when the highest aerosol optical depth (AOD) is recorded (Kim et al., 2007b).

Summer ushers in the southwest monsoon. The slow southwesterly flow typical in the summer make transport from China to Korea favorable, which can dramatically increase the aerosol loading. Stagnant conditions are also more likely to occur in the summer, leading to a locally produced increase in loading.

A majority of the precipitation falls during the months of June and July, during the passage of a quasi-stationary convergence zone, called Changma in Korea. Effects of the summer monsoon in Seoul typically begin between late June and mid-July and last 20-30 days (Chang, 2004). Wet deposition from precipitation efficiently removes aerosol in the boundary layer and decreases the overall aerosol loading. AODs decrease afterwards (Kim et al., 2007b).

Anthropogenic Particulate Matter

In East Asia, there are two dominant types of aerosol particulate matter (PM): mineral dust and anthropogenic pollution. Anthropogenic PM is most common in large cities with the fine-mode size distribution (aerodynamic diameter $<2.5 \mu\text{m}$) (Seinfeld and Pandis, 1998). In Seoul, the chemical composition of fine aerosol near the surface is known to be dominated by organic material (42% of PM_{10} , 34% of $\text{PM}_{2.5}$), likely from anthropogenic sources and secondary formation pathways. An almost equal part is composed of secondary inorganic aerosol like nitrate, sulfate, and ammonium ($\sim 50\%$) (Kim et al., 2018b). Together, these make up about 90% of the total submicron particulate mass and most of the remaining 10% is elemental carbon (also known as black carbon) which is directly emitted soot (Heo et al., 2009; Kim et al., 2018b, 2007a; Kang et al., 2006). Components of anthropogenic PM in East Asia are moderately hygroscopic (Anderson et al., 2003).

Anthropogenic emissions are known to vary with the seasons in this region. Variation is caused mostly by the residential sector as opposed to industry, power, or transportation, which remain relatively constant throughout the year (Ma et al., 2018). In China, a majority of carbonaceous aerosol (elemental and organic) is emitted by the residential sector, a large portion of which is from heating using solid fuel (Ma et al., 2018).

Dust

Dust events exhibit a strong seasonality in Korea, with 87% of dust events occurring in the spring, connected to the typical north-westerly prevailing flow (Kim et al., 2007b; Kim, 2008). In Korea, the predominant sources of dust are the high-altitude deserts in China and Mongolia (Murayama et al., 2001). However, dust generated from roadways and construction is also thought to contribute. From airborne in-situ measurements taken during ACE-Asia, dust was found to be primarily coarse-mode (aerodynamic diameter $>2.5 \mu\text{m}$), nearly non-absorbing and also nearly non-hygroscopic (Anderson et al., 2003).

Biomass Burning

Siberia is a major hotspot for forest fires and the associated aerosol emissions contribute to the aerosol loadings in Korea. In some cases, smoke events are severe enough to create optical depths as large as 4 and elevate surface aerosol concentrations (Jung et al., 2016). However, excluding large events, these sources are fractionally small (~5%) with regard to the overall sources of aerosol in the Korean region (Jeong et al., 2011; Choi et al., 2013). Other potential sources of biomass burning are crop residue burning in the Northern China Plain (NCP) and wood burning in Pyongyang.

Aerosol Optical Depth

The monthly mean of AOD in Seoul reaches a maximum in the summer and minimum in the winter, about 0.65 and 0.25 respectively (Kim et al., 2007b; Panicker et al., 2013; Eck et al., 2005; Ma and Yu, 2015; Nam et al., 2018). The AOD maximum has been attributed to many factors.

Humidification and hygroscopic growth are one significant factor affecting AOD seasonality. The East Asian monsoon causes relative humidity and rainfall to peak in July and August. Precipitation reduces the aerosol loading, but in June the humidity is elevated and loading is still high (Kim et al., 2006, 2007b; Nam et al., 2018). Another factor in AOD seasonality is actinic flux and secondary production. Actinic flux peaks in June and so photochemical activity is high (Kim et al., 2007b; Nam et al., 2018; Buzorius et al., 2004; Yamaji et al., 2006). Wind speed near the surface is also reduced during the summer monsoon. The effect is that the area around sources experience greater aerosol loading, and therefore higher AOD (Kim et al., 2007b).

Surface Particulate Matter

The seasonal variation of AOD is quite large in comparison to the variation in surface concentration of $PM_{2.5}$. Nevertheless, $PM_{2.5}$ also has a seasonal cycle which is opposite to AOD. Peak AOD occurs in the summer, but often the peak $PM_{2.5}$

concentration occurs in the winter. This also seems to be true for most chemical components like sulfate, nitrate, and organic carbon. The only exception is non-sea-salt calcium, which peaks in the springtime when dust transport is highest (Kim et al., 2018a). The important factors driving $PM_{2.5}$ seasonality are boundary layer height, seasonal transport patterns, and wet deposition due to rainfall (Lee et al., 2013; Kim et al., 2018a).

Diurnal Cycle

Both column-based AOD and surface-based $PM_{2.5}$ are thought to exhibit a diurnal cycle. The cycle is a result of cycles in human activity, meteorological variables, and photochemistry. Previous studies in Korea using AERONET have established the basic pattern of peaks in AOD at 9am and 2pm local time and a minimum at noon (Lennartson et al., 2018). However, the HSRL day/night retrievals presented in this thesis indicate a different and strongly seasonal pattern in AOD diurnal cycle.

Air Quality Trends

Recent trends in emissions and air quality in East Asia make characterization of aerosols a moving target, motivating regular monitoring and reevaluation of the state of the science. In the past two decades, Korea has experienced an impressive decline in the surface aerosol concentration (Ahmed et al., 2015; Kim and Lee, 2018). From 2000 to 2015 the annual mean PM_{10} concentration in Seoul declined from $70 \mu\text{gm}^{-3}$ to $40 \mu\text{gm}^{-3}$ (Heo et al., 2017). PM_{10} decreased in six out of seven major cities observed from 1996 to 2010 (Sharma et al., 2014). MODIS AOD retrievals corroborate this decline in aerosol loading, showing a 22% decline in AOD from 2000 to 2010 (Panicker et al., 2013).

Meanwhile, China's $PM_{2.5}$ concentrations have increased from 1999 to 2011 (Peng et al., 2016). Annual mean AOD had a similar increase from 2000 to 2007 (Qin et al., 2018). Such anthropogenic changes can be expected to alter many aspects of the aerosol climatologies previously established in the region including chemical composition, seasonality, vertical distribution, and amount.

Poor air quality in Korea has been partially attributed to transport of aerosol and gaseous precursors from China; however, there is still much uncertainty due to the difficulty of establishing such a causal link. That said, in a modeling study, Kim et al. (2017b) found that 60% of Seoul's surface particulate matter was attributable to foreign emissions, and other modeling studies have found similar results (Koo et al., 2008; Kim et al., 2017a).

Trends in air quality can also be attributed to changing climate. Kim et al. (2017c) found that recent decreases in mean wind speed since 2012 have reversed past improvements in air quality in Seoul.

1.3 Overview of Aerosol Observations

The novel observations made by the UW-Madison HSRL are a core component of this thesis. In this section, the state of aerosol observations is summarized with emphasis on the particular strengths and weaknesses inherent to each instrument.

Passive aerosol remote-sensing

The state-of-the-art instrumentation for aerosol remote-sensing are ground-based sun-photometers and satellite visible imagers. AERONET and MODIS are the most common remote-sensing platforms used for both forecasting and analysis. Passive observations from ground (AERONET) or from space (MODIS) are limited to only column aerosol optical properties and cannot be made at night or in cloudy scenes. The AERONET instrument has a global network, but only provides information at discrete locations. Satellite imagers such as MODIS provide global coverage; however, unlike AERONET, MODIS cannot observe the diurnal cycle of aerosol properties because it is in a sun-synchronous orbit with overpasses at the same local time every day. The recent launch of Himawari-8 and GOCI geostationary satellites with coverage in Asia provide similar spectral measurements to MODIS but with continuous 10 minute observations. However, as with the LEO imagers the AOD retrieval only provides the total column AOD for cloudless, daytime observations,

and potentially suffers from selection bias, as AOD, day-length, and cloudiness co-vary with the seasons (Eck et al., 2018).

Lidar aerosol observation

Active sensors like the UW-Madison HSRL are able to resolve vertical distributions of aerosol optical properties, can operate day and night, and are not limited to cloudless scenes. In this thesis, HSRL data is collected in a single location in Seoul, South Korea.

The UW-Madison HSRL is not the only lidar technology deployed in the region. Micropulse lidars and multiwavelength Raman lidars are able to make similar measurements of backscatter. However, micropulse lidar retrievals require assumptions regarding the atmospheric lidar ratio profile and instrument calibration. Furthermore, the signal-to-noise ratio (SNR) is much lower compared to the HSRL. Raman lidars produce very noisy data during the day when the inelastic scattering signal is weak compared to the solar background. In comparison, the UW-Madison HSRL is a much more capable technology, able to make well-calibrated observations at any time of the day.

In-situ observation

Remotely-sensed AOD is only one measurement of aerosol properties, and correlates well with poor visibility. Sometimes, like during dust or smoke outbreaks, AOD is increased, but most of the particulate matter is aloft. At other times (e.g. winter), AOD is minimal but particles are concentrated near the surface. This is partly because concentration of aerosol near the surface depends much more on the height of the boundary layer (Zhang et al., 2009; Quan et al., 2013; Qu et al., 2016; Lee et al., 2013). The dry mass concentration of particulate matter having an aerodynamic diameter less than 2.5 microns ($PM_{2.5}$) at the surface has become a standard measurement for determining risk to public health (Harrison and Yin, 2000). The danger is sometimes sufficient to warrant emergency measures such as free public

transport in Seoul in January 2018 (Coffey, 2018). For this reason, continuous in-situ aerosol measurements of $PM_{2.5}$ are common in large cities.

Common Limitations

Interactions between aerosols and clouds are difficult to measure, in-part due to the inability of most remote sensing instruments to observe cloudy scenes. The challenge with observing cloudy scenes with passive instrumentation is not only the obvious obscuration, but also the 3D radiative effects of scattering near the cloud, which foils passive retrievals typically used for aerosol properties (Várnai and Marshak, 2009). This is not a worry for an active instrument like the UW-Madison HSRL or CALIOP, which makes these instruments important supplements to passive instrumentation. Confusion between clouds and thick haze aerosol is another problem that afflicts both passive and active aerosol measurement in East Asia (Shi et al., 2014). There is also the possibility of that thin cirrus, undetected by cloud screening, can contaminate aerosol retrievals.

As a result of aerosol remote sensing being dominated by column-based measurements, data on the vertical distribution of aerosol in the atmospheric column is limited. The space-based lidar CALIOP is the only global measurement capable of resolving vertical distribution, but it is still limited by low SNR and a sun-synchronous orbit, limiting diurnal sampling. The paucity of information on vertical structure impacts modeling efforts and the task of estimating surface concentrations from the available column-only remote sensing data like MODIS or AERONET (Toth et al., 2019).

KORUS-AQ

In March of 2016, the UW-Madison HSRL was deployed on the campus of Seoul National University in Seoul, South Korea for the KORUS-AQ field campaign, an international collaboration between Korea and the US to study air quality in the region. Aside from the UW-Madison HSRL, airborne measurements from the NASA DC-8, ground-based in-situ and remote sensing, and satellite measurements

participated. Despite the intensive operations only lasting approximately one month, the UW-Madison HSRL remained operational for almost 2 years, until the laser began experiencing issues in February 2018.

Funded by NASA, the primary objectives of KORUS-AQ relate to identification of the factors controlling air quality on the Korean Peninsula. Secondary formation of aerosol and point source emissions were of particular interest. The months (May-June) for intensive operations were specifically chosen to maximize transport of pollutants and photochemical processes. Weather conditions were mostly stagnant during the experiment. One exception was the period from May 25-28, where conditions allowed direct transport from China; this coincided with the most prominent of the few days where Korean $PM_{2.5}$ standards were exceeded during the experiment.

Considering the large influence of weather on air quality and the variability of weather conditions, such a short experiment cannot be considered automatically representative. The role of the UW-Madison HSRL is to provide high-quality, vertically resolved measurements of aerosol above Seoul, as a long-term seasonal context for the intensive observations conducted in the area.

2 METHODS

HSRL Theory

Lidars work by generating a light pulse and recording the scattered light and time-of-flight, which allows the range associated with the light measurement to be known. The power of the scattered light follows the inverse-square law, whereby the signal becomes quadratically smaller with distance. Lidars also have to contend with non-negligible attenuation by air molecules and aerosol. For the UW-Madison HSRL design, the combination of these with the power of the laser and the tenuous scattering material, limit the backscattering to only a few photons per range bin in the best case. Thus, the detector must be sensitive enough to count individual photons and many laser pulses must be accumulated before the average becomes statistically representative. The HSRL used in these analyses uses solid-state avalanche photodiode detectors which can sample every 50 ns. The laser pulses at 4000 Hz and the data acquisition system accumulates photon counts every 2.5s. Even after a great deal of temporal aggregation, the data rate is far superior to every other instrument included in this thesis.

The HSRL technique is different than a typical backscatter lidar because it is able to separate the scattering from gas (molecular) and aerosol. This is possible because the atmospheric Rayleigh scattering is Doppler-broadened much more than the aerosol scattering. The separation of the two scattering spectra requires a high spectral-resolution notch filter furnished by an absorption line of gaseous iodine (Razenkov, 2010; Holz, 2002; Grund and Eloranta, 1991; Piironen and Eloranta, 1994). The definition of backscatter coefficient and depolarization are given in Equations 2.1 and 2.2, respectively. The detection system and radiative transfer are represented in Equations 2.3-2.5, one equation for each detector.

$$\nu = \beta_s \frac{P(\cos\pi)}{4\pi} \quad (2.1)$$

$$\delta = \frac{v^\perp}{v^\parallel} \quad (2.2)$$

$$\frac{\delta S_c^\parallel}{\delta t} = \frac{N_0 c A}{2r^2} G(r) e^{-2\tau(r)} \left[\eta_{ac}^\parallel v_a^\parallel(r) + \eta_{mc}^\parallel v_m^\parallel(r) \right] + S_{bc}^\parallel \quad (2.3)$$

$$\frac{\delta S_m^\parallel}{\delta t} = \frac{N_0 c A}{2r^2} G(r) e^{-2\tau(r)} \left[\eta_{am}^\parallel v_a^\parallel(r) + \eta_{mm}^\parallel v_m^\parallel(r) \right] + S_{bm}^\parallel \quad (2.4)$$

$$\frac{\delta S_c^\perp}{\delta t} = \frac{N_0 c A}{2r^2} G(r) e^{-2\tau(r)} \left[\eta_{ac}^\perp \delta_a v_a^\parallel(r) + \eta_{mc}^\perp \delta_m v_m^\parallel(r) \right] + S_{bc}^\perp \quad (2.5)$$

$$v_a^\parallel = \frac{\eta_{mm}^\parallel \left(\frac{\delta S_c^\parallel}{\delta t} - S_{bc}^\parallel \right) - \eta_{mc}^\parallel \left(\frac{\delta S_m^\parallel}{\delta t} - S_{bm}^\parallel \right)}{\eta_{ac}^\parallel \left(\frac{\delta S_m^\parallel}{\delta t} - S_{bm}^\parallel \right) - \eta_{am}^\parallel \left(\frac{\delta S_c^\parallel}{\delta t} - S_{bc}^\parallel \right)} v_m^\parallel = S_r^\parallel v_m^\parallel \quad (2.6)$$

$$v_m = \alpha_{back} \rho \quad (2.7)$$

In Equation 2.6, parallel aerosol backscatter coefficient (v_a^\parallel) is solved in terms of parallel molecular backscatter coefficient (v_m^\parallel). Note that the solution is independent of optical depth, overlap function, laser power, range, and telescope size. The molecular backscatter has a constant depolarization ratio and the molecular backscatter coefficient depends only on the gas density (Equation 2.7), which can be calculated using an atmospheric profile (Razenkov 2010). The main effect of the iodine filter is to make $\eta_{am}^\parallel \ll \eta_{ac}^\parallel$ by filtering most aerosol backscatter from the molecular channel and thus make the scattering ratio (S_r) computation (Equation 2.6) well-conditioned.

Including the solution for aerosol and molecular backscatter, aerosol depolarization in Equation 2.5 can be solved for in a similar manner by dividing Equation 2.5 by Equation 2.3.

$$\tau(r) = \int_0^r \beta_e(r') dr' \quad (2.8)$$

Table 2.1: Description of symbols

Symbol(s)	Description
r	range
$\nu_a^{\parallel}, \nu_a^{\perp}$	parallel and perpendicular aerosol backscatter coefficient
τ	optical depth
δ_a	aerosol particle depolarization
N_0	number of transmitted photons
A	area of telescope receiver
c	speed of light
$G(r)$	geometric overlap function
$\frac{\delta S_c^{\parallel}}{\delta t}, \frac{\delta S_m^{\parallel}}{\delta t}, \frac{\delta S_c^{\perp}}{\delta t}$	detected photon count rate: combined parallel, molecular parallel, combined perpendicular
$S_{bc}^{\parallel}, S_{bm}^{\parallel}, S_{bc}^{\perp}$	detected background photon count rate
$\eta_{ac}, \eta_{am}, \eta_{mm}$	calibration parameters
η_{mc}	
$\beta_s, \beta_e, \beta_{e,a}$	scattering coefficient, extinction coefficient, aerosol extinction coefficient, and molecular extinction coefficient
$\beta_{e,m}$	
α_{back}	mass backscattering coefficient

$$\beta_e(r) = \frac{1}{2} \frac{\partial}{\partial r} \log G(r) \frac{\frac{N_0 c A}{2r^2} (\eta_{am}^{\parallel} \nu_a^{\parallel}(r) + \eta_{mm}^{\parallel} \nu_m^{\parallel}(r))}{\frac{\delta S_m^{\parallel}}{\delta t} - S_{bm}^{\parallel}} \quad (2.9)$$

Extinction can also be derived as shown in Equation 2.9. However, the range-dependent overlap function (G) must be supplied. Co-axial backscatter lidars often have unity overlap above ~ 0.5 km (Takeuchi and Sato, 1987; Vande Hey et al., 2011; Mao et al., 2012). However, the UW-Madison HSRL uses a much narrower field-of-view telescope which raises the unity overlap level to over 5km; the values of the overlap function below this are highly uncertain without additional information. Estimation of the overlap function is possible with a second molecular channel having a wide field-of-view (WFOV) (Eloranta, 2014). More details on the estimation process are provided in the HSRL molecular extinction methodology section.

HSRL Calibration Challenges

A practical implementation of the HSRL requires estimating all of the calibration parameters (η_{ij}) in equations 2.3-2.5. For example, the spectra of molecular return changes with pressure and temperature of the scattering gas; so, the fraction of molecular spectra which are filtered (η_{mm}^{\parallel}) changes with the range-dependent pressure and temperature. Proper estimation of this parameter is done by measuring the iodine absorption line and finding the transmission of simulated spectra. But, this is made more difficult by the solar background filter which modifies the transmission of the wider molecular spectra by varying amounts depending on the density of the gas in the etalon chamber. Additional complications involving nonlinear and range-dependent detector response (not in equations) can also affect measurements (Razenkov, 2010).

Aerosol Extinction vs. Aerosol Backscatter Coefficient

There are significant advantages to an optical depth and extinction retrieval over (or in addition to) the traditional backscatter retrieval. A majority of non-lidar aerosol measurements are passive, and all passive aerosol measurements measure optical depth or extinction, directly or indirectly (e.g. AERONET, MODIS, MISR, visibility). Accordingly, most aerosol models diagnose extinction for assimilation and evaluation (Lynch et al., 2016; Liu et al., 2011; da Silva, 2011). So, comparison with non-lidar measurements or models often must be done in extinction space. Aerosol extinction is also of greater scientific interest than aerosol backscatter coefficient. Only extinction can be used to derive direct aerosol radiative effect, which is needed in climate analyses. Extinction is also better correlated with aerosol particulate properties like total cross-sectional area and scattering coefficient than backscatter. It is also more appropriate when analyzing hygroscopicity. Comparing extinction-to-backscatter ratios (lidar ratio) has also been used for aerosol typing because it depends on aerosol shape, size, and composition, but not concentration.

Although the UW-Madison HSRL can measure backscatter very accurately, the current science objectives demand calibrated measurements of extinction for either

direct application or derivation of extinction-to-backscatter ratio (lidar ratio).

Aerosol Lidar ratio

The ratio of aerosol extinction ($\beta_{e,a}$) to aerosol backscatter coefficient, usually referred to as the aerosol lidar ratio (S_a), is known to vary between about 20 to 80 sr for bulk aerosol mixtures, though the true range may be larger. It reflects the shape, size, and composition of individual aerosol particles, independent of the number concentration. For example, isotropic non-absorbing scatterers will have a lidar ratio of 4π (12.6) sr.

The lidar ratio of a column of atmosphere may be computed as either the arithmetic mean of the lidar ratio of infinitesimal layers (Equation 2.10) or as a bulk value (Equation 2.11). The bulk lidar ratio approximation of mean lidar introduces uncertainties by differently weighing volumes based on extensive optical properties. However, empirical comparison of the two will show that bulk lidar ratio is a good approximation of the mean boundary-layer lidar ratio.

$$\overline{S_a} = \frac{1}{z_{\text{top}}} \int_0^{z_{\text{top}}} \frac{\beta_{e,a}(z)}{\nu_a(z)} dz \quad (2.10)$$

$$S_{a,\text{bulk}} = \frac{\int_0^{z_{\text{top}}} \beta_{e,a}(z) dz}{\int_0^{z_{\text{top}}} \nu_a(z) dz} \quad (2.11)$$

Aerosols usually exist as a complex mixture of shapes, sizes, and compositions. Because nearly all scattering occurs within the Mie resonance regime, the phase function and backscattering efficiencies of spherical particles of a single size oscillate over a wide range as size changes. Non-spherical particles like mineral dust introduce even more difficulty. Dust shape has been found to reduce backscatter by $\sim 2.5\times$ as compared to a spherical particle, but extinction is not as significantly affected (Barnaba and Gobbi, 2001; Mishchenko et al., 1997; Yu et al., 2010). As a result, any given lidar ratio is difficult to predict heuristically or interpret without additional information. Inorganic aerosols are often assumed to have a single scatter albedo near one, which should result in moderate lidar ratios with most

variation occurring due to shape and size. On the other hand, black carbon has a single-scattering albedo less than 0.25, meaning that the lidar ratio is about 4 times larger, phase function being equal. As it ages, black carbon can accumulate an organic carbon shell and this internal mixture may result in lensing which further increases the absorption efficiency and therefore the lidar ratio (Zhang et al., 2018).

Relative humidity is also a consideration with lidar ratio. Particles that uptake water could change in both size, shape, and index of refraction and therefore lidar ratio. However, it is not obvious whether the effect is monotonic or uniform between particle types. The consensus of several theoretical studies is that humidified aerosols increase lidar ratio. Ackermann (1998) and Su et al. (2008) analytically showed a large increase in continental aerosol lidar ratio (± 20 sr) with greater relative humidity. However, clouds generally have lower lidar ratios than continental aerosol at any RH (Ansmann et al., 1992; Pinnick et al., 1983; Kuehn et al., 2016). Clearly, any monotonic relationship between RH and lidar ratio breaks down once particles reach droplet size (diameter >10 μm).

Observations of aerosol lidar ratios using a Raman lidar in Gwangju, Korea found the average lidar ratio at 532 nm in the spring to be 56 ± 9 sr and 63.1 ± 12.8 sr in the autumn. Asian dust had lower values of 51 ± 6 sr, and smoke had higher values 65 ± 8 sr (Noh et al., 2008). In Seoul, the mean lidar ratio was measured to be 56 ± 18 in winter, 57 ± 16 in spring, 62 ± 15 in summer, and 61 ± 16 in fall (Nishizawa et al., 2017). A separate study in Seoul found an annual mean of 60.44 ± 23.17 sr (Kim et al., 2015). In summary, the intra-seasonal variation in lidar ratio is far greater than seasonal variation, but the seasonal peak is expected to be near the end of summer when there is less dust, the fraction of carbonaceous to inorganic aerosol is the greatest, and relative humidity is greatest.

HSRL measurements of the Lidar Ratio

The bulk lidar ratio for the column can be well characterized when the total aerosol extinction is known, often through independent measurement by nearby sun-photometer. A constant lidar ratio with this value is often assumed for standard

backscatter lidars to complete a simultaneous retrieval of backscatter and extinction (Fernald et al., 1972). However, this is not a good assumption, as there is no reason to expect a constant lidar ratio with altitude and any deviation from the average lidar ratio will result in systematically inaccurate retrievals. Indeed, measurement of lidar ratio is possible, though difficult, using the molecular channel of the HSRL, and results will show systematic vertical gradients in lidar ratio. Direct extinction measurement notwithstanding, assuming a lidar-ratio on HSRL data is still an improvement. Because the HSRL technique measures aerosol backscatter independently, incorrect lidar ratio assumptions do not accumulate down-range like they would with a standard backscatter lidar. In summary, extinction can be retrieved with the HSRL using either the molecular signal or a lidar ratio assumption to convert from aerosol backscatter to aerosol extinction coefficient.

HSRL sensitivity to aerosol

All of the UW-Madison HSRL measurements presented in this thesis are at 532 nm wavelength. At this wavelength, particles with size parameter of 1 are about 150 nm in diameter which marks the approximate lower limit of sensitivity for aerosol backscatter coefficient. The aerosol backscatter coefficient is also dependent on the complex index of refraction of the particles. For most particulate matter the imaginary component is nearly zero and the particles are non-absorbing at 532 nm. An exception is black carbon, which is strongly absorbing.

Hygroscopic growth is another factor to consider, as this changes both the index of refraction and optical size. The hygroscopicity of different aerosols varies greatly, where water-soluble inorganic ions like sulfate will readily absorb water but the crustal material that constitutes dust is hydrophobic. Little can be done to predict hygroscopic growth of complex mixtures of aerosol components prior to measurement and these effects will be apparent in the optical data analyzed. On the other hand, $PM_{2.5}$ samples are desiccated prior to measurement.

Regarding particle size distribution, remote-sensing measurements will be most sensitive to changes in cross-sectional area per volume. But, this area (proportional

to surface area for spheres) will either overrepresent small particles per their mass or underrepresent small particles per their number. Mass is more important in applications like emission inventories, air quality, chemistry, and forecasting. Number is more important in applications related to aerosol-cloud interactions. These differences need to be considered when applying remote-sensing observations across domains, as in this thesis, and when changing particle size distributions are a possibility.

Observations other than aerosol backscatter coefficient are available from the UW-Madison HSRL in Seoul. The UW-Madison HSRL transmits a linearly polarized beam and has a 532nm cross-polarization channel from which average particle linear depolarization ratio is measured. Particle linear depolarization ratio is defined as the ratio of perpendicular-polarized aerosol backscatter to parallel-polarized aerosol backscatter of a single particle, and this records the general sphericity of the specimen. For example, crystallized sea-salt is known to have a higher particle linear depolarization ratio than spherical deliquesced sea-salt droplets (Sakai et al., 2010).

The optical properties of dust are high depolarization and relatively small Angstrom exponent. These properties can identify dust with high contrast in lidar data; however, because of similarities with cirrus, additional parameters such as texture and morphology must be considered when cloud-screening. The particle linear depolarization ratio of Asian dust published in the literature tends toward 35% (Sugimoto et al., 2003; Shimizu et al., 2004). On the other hand, the lidar-observable optical properties of anthropogenic aerosol like organic carbon, sulfate, nitrate, and biomass burning smoke are similar. All have low depolarization and high Angstrom exponent.

Aerosol Modeling

The Navy Aerosol Analysis Prediction System (NAAPS) model is a semi-Lagrangian aerosol model designed to assimilate AOD measurements made by MODIS, among other observations. There is a single size bin for each of the four aerosol species. The

bulk approximation used for converting between mass concentrations and optical extinction is relatively simple (Lynch et al., 2016). The meteorology is supplied by another Navy model, the Navy Global Environmental Model (NAVGEM). In this thesis, reanalysis output is every 6 hours and is subset to 2016-05-01 to 2017-04-30, the same time period as the HSRL dataset.

For analysis of the UW-Madison HSRL data, relative humidity needs to be estimated. This meteorology data is sourced from the ECMWF ERA5 hourly reanalysis, linearly interpolated to the UW-Madison HSRL location and times (C3S, 2017).

AERONET

The AERONET sun-photometer network has been one of the most impactful observing systems on aerosol research. There is an operational AERONET instrument located on the SNU campus, the same campus as the UW-Madison HSRL. The high quality of the colocated AERONET data encourages comparison. The new version 3 of the AERONET level 2.0 product and SDA retrieval are used.

University of Wisconsin HSRL

The UW-Madison Arctic HSRL was operational in Seoul from March 7, 2016 to February 24, 2018; data is available at http://hsrl.ssec.wisc.edu/by_site/26/a11/2018/02/24/. Only a single annual cycle can be fully represented, so a subset from May 1, 2016 to Apr 30, 2017 is used for this thesis. The UW-Madison HSRL in Seoul was located 104 m above mean sea-level. In a cloudless scene the usable data ceiling is over 15 km AMSL. This ceiling is far beyond the range containing a vast majority of aerosols that are radiatively significant or relevant to air quality. Instead, only observations below 10 km are considered relevant in this thesis. During HSRL data processing, vertical averaging of photon counts is not performed beyond the raw acquisition limits of 7.5 m. Temporal averaging is required to reduce photon counting noise, but is limited to 1 minute such that boundary layer eddies, which often enhance aerosol backscatter and extinction, are preserved. A near-surface

aerosol backscatter coefficient is computed by averaging between 150 m and 300 m AMSL.

HSRL molecular extinction

Measurement of extinction is possible with the HSRL as shown in the Equation 2.9. But, an overlap function must be supplied. For this dataset, the overlap is estimated hourly using the WFOV molecular channel. First, all the HSRL data is denoised by averaging temporally for 2 hours. From the denoised molecular WFOV profile, extinction is estimated as in Equation 2.9, but the overlap function (G) is known to be unity above ~ 0.5 km. With knowledge of the extinction and optical depth ($\tau(r)$), Equation 2.4 can be solved for the overlap function (G). This process is repeated for every hour having no clouds below 10km for at least 2 hours. The resulting overlap was observed to have strong diurnal oscillations. For times when clouds prevent the overlap from being computed, the overlap is imputed by forward filling the previous overlap function for that hour of the day. Below 500 m the overlap cannot be corrected, so the additional AOD is estimated by integrating backscatter to 500 m and multiplying by the same interpolated bulk lidar ratio as the rest of the AOD estimates.

HSRL-based AOD

For compatibility with AERONET, there needs to be a vertical integrated AOD derived from UW-Madison HSRL data. The most desirable AOD would be derived from the HSRL molecular scattering, which will be referred to as the molecular AOD. As explained before, at this time the molecular AOD has high systematic uncertainties due to the uncertain overlap, so it will be supplemented by AOD estimates where column-integrated aerosol backscatter coefficient will be converted to AOD by assuming a bulk lidar ratio. The AERONET AOD will be used to determine the true bulk lidar ratio whenever AERONET observations are available. This instantaneous estimate is noisy and instead the mean value of every month is linearly interpolated. This interpolation can be extended to the entire UW-Madison

HSRL dataset. Of course, the direct matchup cannot be systematically biased, but cases where AERONET observations are impossible, like at night or under high cloud cover, could have a consistently different lidar ratio. Accepting this possibility, a range of UW-Madison HSRL AOD subsets with differing sampling are provided. The aim is to tradeoff uncertainty in lidar ratio for more complete coverage.

The most certain UW-Madison HSRL AOD subset is directly matched one-for-one with AERONET. Figures 2.1 and 2.2 validate the molecular AOD and lidar-ratio estimated AOD with AERONET ground truth. The results show that the lidar-ratio estimated AOD agrees the best with AERONET, but the molecular AOD also has a median absolute error less than 0.05 across all seasons. The lidar-ratio estimated AOD performs much better than molecular AOD during low AOD conditions (Fig. 2.1) because the small attenuation of the molecular signal is harder to detect than the backscatter signal, which is easily detected. In high AOD conditions (Fig. 2.2), both seem to perform similarly. Recall that the lidar-ratio-estimated AOD was fit to AERONET, but only once per month. The lower error variance clearly demonstrates skill not attributable to just being unbiased. To conclude, the central concern regarding the estimation of AOD using aerosol backscatter coefficient is bias during scenes underrepresented or unobserved by AERONET, but performance otherwise is excellent. With the molecular AOD, higher variance and systematic bias related to the instrument overlap is the main source of error.

The next most constrained retrieval uses all UW-Madison HSRL scenes without clouds below 10km. All scenes containing water clouds and cirrus below 10 km will be filtered out, but unlike the AERONET matchup subset many more observations between AERONET observations (at a maximum rate of 1/min) and at night will be included. The next tier only integrates clear scenes up to 5km, which allows cirrus but may reduce AOD a little by excluding very high aerosols.

Manual HSRL Cloud Masking

Clouds, while technically aerosols, are generally regarded to be separate phenomena and must be masked out prior to analysis. Precipitation also must be masked.

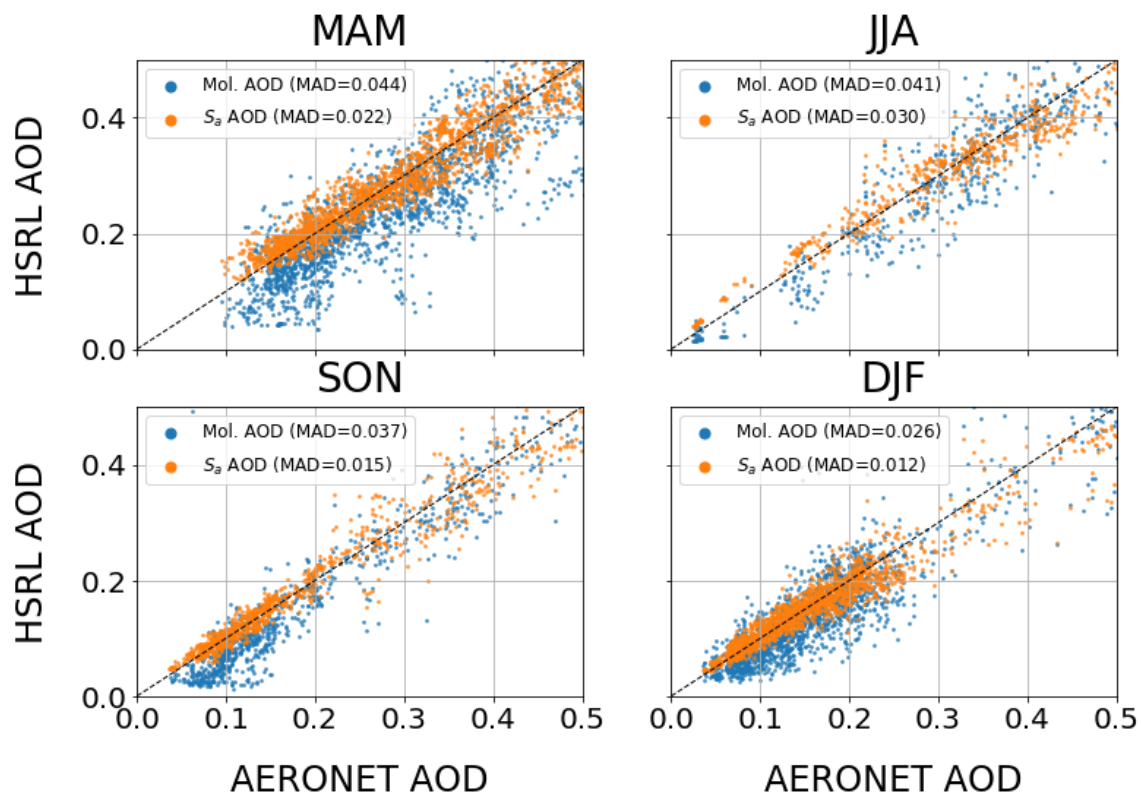


Figure 2.1: Two methods of estimating column AOD are validated using AERONET as ground-truth. The first method in blue (Mol. AOD) uses the geometrically-corrected HSRL molecular signal to determine optical depth and is independent of AERONET. The second method in orange (S_a AOD) is computed by integrating aerosol backscatter and fitting a lidar ratio to AERONET for each month and linearly interpolating these to the actual time resolution. This figure shows the low-AOD range and the Fig. 2.2 shows the high-AOD range. Median absolute difference (MAD), including data for larger AOD, is shown in the legend as a performance metric.

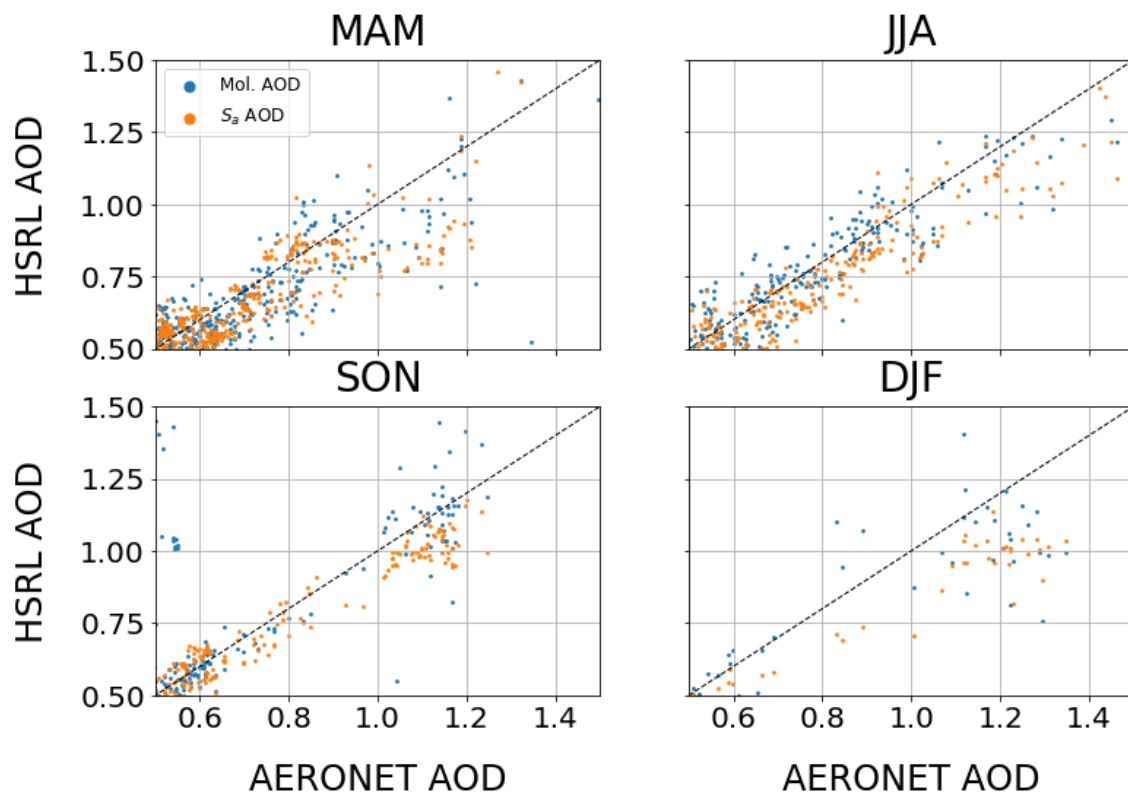


Figure 2.2: Similar to Fig. 2.1, but scale shows high-AOD range.

Automatic masking is difficult because aerosol, cloud, and precipitation sometimes have similar optical properties. The author elected to manually cloud-clear the dataset. This was accomplished using the tools provided by Zooniverse to draw rectangular boxes to cover clouds and precipitation on RGB images of the dataset. An example of both is shown in Figure 2.3. The dataset was divided into 5 km altitude and 8 hour duration segments to enhance control and resolution during the manual clearing. Clouds are highly scattering and optically thick, therefore they may overly-attenuate the beam. Therefore, any measurements made above a cloud or virga are questionable and masked regardless of existing quality control flags.

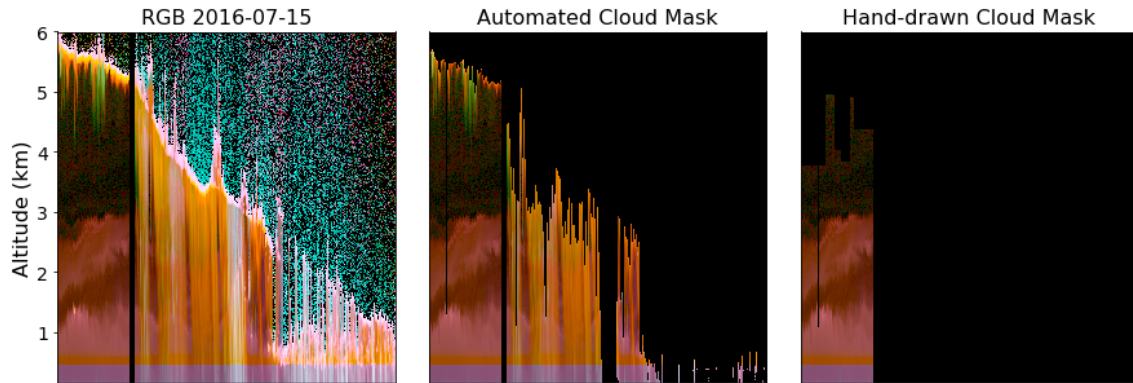


Figure 2.3: An example day of cloud-masking HSRL data with altitude on the y-axis and time on the x-axis. The image is an RGB combination of aerosol backscatter coefficient, aerosol depolarization ratio, and color ratio. Water clouds and precipitation are colored orange and ice clouds are green. In this example, automated cloud-masking misses the precipitation and cloud edges. The color band near the surface is caused by the limitations of the near-surface 1064 nm channel.

Separating dust from smoke/pollution using linear depolarization

The contribution of dust to aerosol backscatter coefficient (ν_d) can be estimated by leveraging the assumed particle linear depolarization ratios of dust (δ_d) and non-dust (δ_{nd}) (Tesche et al., 2009). Equation 2.12 is the definition of depolarization ratio in terms of dust and non-dust backscatter coefficients. Equation 2.12 solved for dust backscatter coefficient is shown in Equation 2.13 and non-dust is the remainder (Equation 2.14). Here, based on previous studies of Asian dust, the assumed particle linear depolarization of dust is 35% (Sugimoto et al., 2003; Shimizu et al., 2004). The particle depolarization of non-dust varies depending on study, hygroscopicity, and composition. Most studies conclude that non-dust depolarization is small but nonzero (<5%). Here, it is assumed to be negligible. Deviations of dust from the assumed depolarization (35%) are likely and represent a more significant source of error. In any case, the performance will be validated in the results section using the AERONET SDA retrieval of coarse-mode AOD.

$$\delta_p = \frac{\nu_a^\perp}{\nu_a^\parallel} = \frac{\nu_d^\perp + \nu_{nd}^\perp}{\nu_d^\parallel + \nu_{nd}^\parallel} \quad (2.12)$$

$$\nu_d = \frac{(1 + \delta_d)(\nu_a^\perp - \delta_{nd}\nu_a^\parallel)}{\delta_d - \delta_{nd}} \quad (2.13)$$

$$\nu_{nd} = \nu_a - \nu_d \quad (2.14)$$

3 RESULTS AND DISCUSSION

Lidar Ratio

By matching up AERONET AOD and UW-Madison HSRL's integrated aerosol backscatter coefficient, a bulk lidar ratio for the column can be derived. Figure 3.1 shows the aggregation of the ratio by month (not weighted by backscatter). Both AERONET and the UW-Madison HSRL can be used to determine the AOD. The UW-Madison HSRL and AERONET combination should be regarded as the best estimate, but the UW-Madison HSRL alone captures the same trends.

As discussed previously, explaining the variation in lidar ratio is difficult due to the complex interpretability of lidar ratio and the many possible factors which are known to vary by season. We find that during spring time the median value of the bulk lidar ratio is at a minimum likely representing the increased frequency of Asian dust. However, the lidar ratio is also lower during the winter months with values consistent with dust, yet there must still be a significant non-dust component in the winter. Relative humidity is another possible cause of lidar ratio changes, involved when hygroscopic growth changes particulate size and refractive index. Season is a confounding variable between RH and other possible explanations, like different emission sources, actinic flux, transport, or composition. Therefore, to show that RH is influencing lidar ratio, care must be taken to control for season. Figure 3.2 shows a weak relationship between backscatter-weighted column RH and bulk lidar ratio. The slope of the best fit is robust between seasons, except for JJA, when lidar ratio is even more sensitive to changes in RH. At these short timescales the coefficient of determination is small, suggesting that RH is by no means the only source of variation. Nevertheless, the inter-seasonal changes in bulk lidar ratio are modest enough (± 8 sr) that even this weak relationship with RH can explain almost all of the seasonal variation in bulk lidar ratio.

To proceed with analysis in later parts, some time-varying lidar ratio must be selected. All estimation of AOD or extinction in this thesis (including Figures 2.1 & 2.2), unless otherwise specified, used a lidar ratio interpolated from these monthly

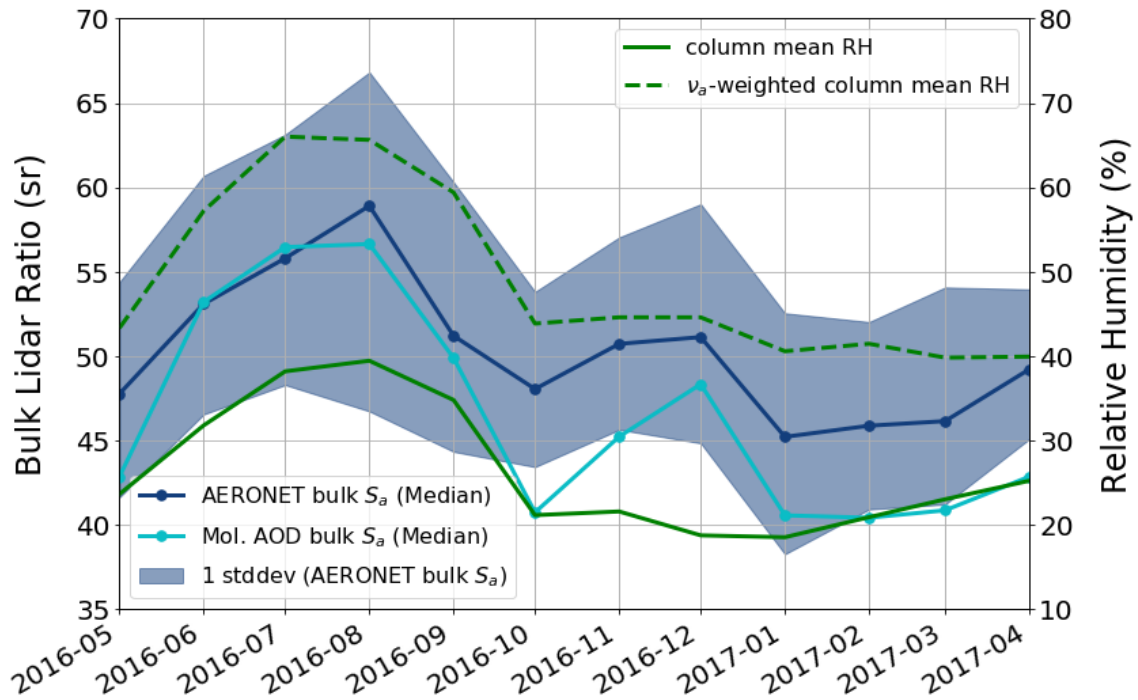


Figure 3.1: Time-series of monthly bulk lidar ratio. The bulk lidar ratio is computed using both the AERONET and HSRL-derived AOD (the numerator). In dark blue is the AERONET-based mean and a fill indicating 1 standard deviation. In light blue is the mean based on the geometrically-corrected HSRL molecular signal, which includes a both day and night retrievals compared to the day-only AERONET. For comparison, two average relative humidities from ERA5 are also plotted. One is a simple column average, the other is vertically-weighted by HSRL aerosol backscatter.

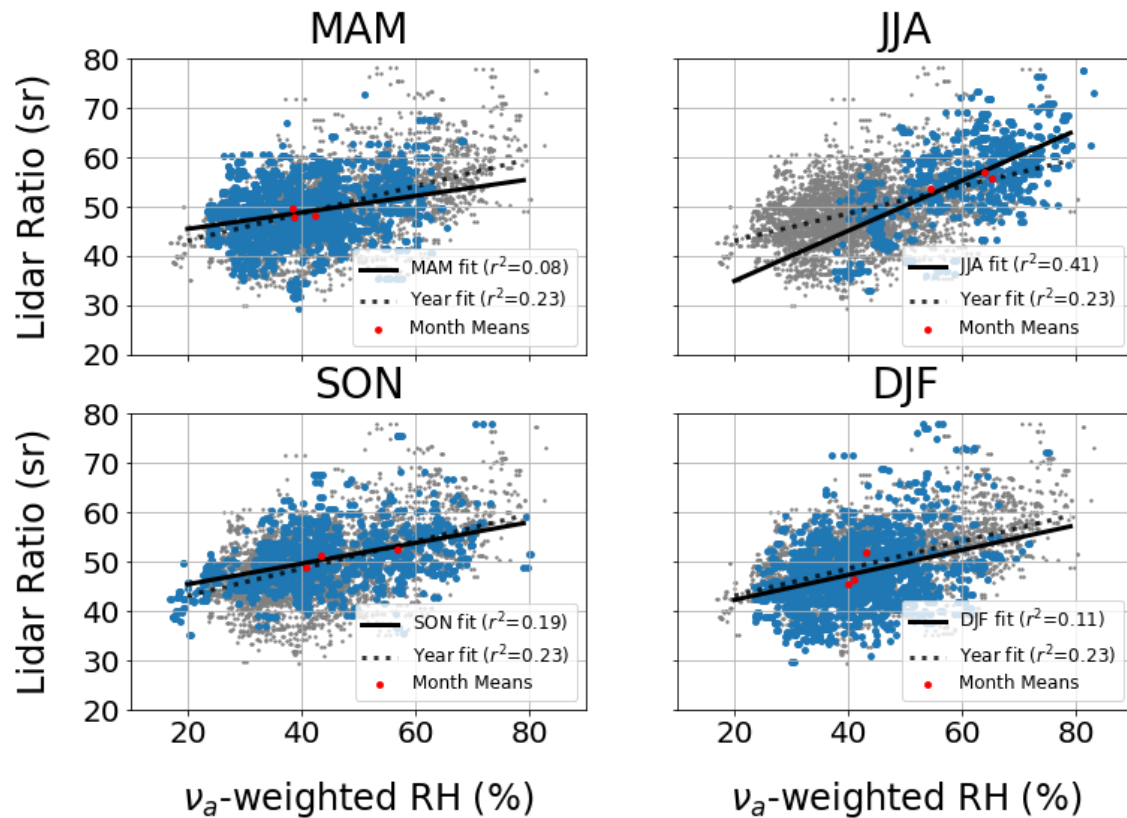


Figure 3.2: The AERONET-based lidar ratio and backscatter-weighted relative humidity averaged every 20min are plotted for each season. A linear fit was computed for each season and for the entire year. The monthly-mean values are also plotted in red.

mean lidar ratios.

Seasonal Cycle

Using lidar ratio, we have several estimations of the monthly-mean AOD from the UW-Madison HSRL aerosol backscatter coefficient, all of which roughly match the priors (details in review section) of high AOD in the summer and low AOD in the winter. The differences between identically-sampled HSRL AOD (Fig. 3.3a blue line) and AERONET AOD (black line) have been removed (green dots) by

adjusting the lidar ratio.

Figure 3.3b expands the sampling to nighttime and cloudy scenes. Note that these differences in AOD are all only due to changing sampling behavior. The HSRL mean of AOD in scenes without clouds in the first 10km is labeled “Cloudless”. “Cloudless” includes nighttime observations, cases with high cirrus, and has a much greater observation rate than the AERONET matchup. The HSRL AOD derived from the corrected molecular channel does not assume a lidar ratio, but it has uncertainty from the overlap function, which is known to be highly dependent on time of day if uncorrected. It is sampled the same as (and agrees very well with) “Cloudless”. Because most of the variation is expected to occur within the boundary layer, the lowest 5km (“Cloudless 5km”) should sufficiently represent most variation and also include cases with just cirrus or high water clouds. It excludes some high-altitude aerosol and therefore has a low bias.

The most extreme disagreement between AERONET and HSRL AOD occurred in September, where the AERONET median significantly underestimated the median AOD when sampling behavior is changed. This is because the transition from the high summer optical depths to low winter optical depths occurs in September and the distribution of AOD is somewhat bimodal. The AERONET median finds the lower mode while the UW-Madison HSRL median finds the high mode. So, despite the difference in median values, the AERONET and UW-Madison HSRL interquartile ranges agree. A potential future experiment would be to compare multiple AERONET sites and lidar data to determine whether this difference is systematic or peculiar to 2016.

As will be shown in the diurnal results (Fig. 3.4), AODs are generally smaller at night than during the day. Therefore, AERONET AOD was expected to be higher than the HSRL AODs, which include nighttime; but, there is no significant bias even in the summer. One possible reason is that mean daytime AOD is not significantly higher than mean nighttime AOD, although the peak AOD occurs during the day. Another reason is that that higher cloud amounts during the day are selecting for cloudless scenes having lower AERONET AODs. This cancels the high bias of daytime-only observations.

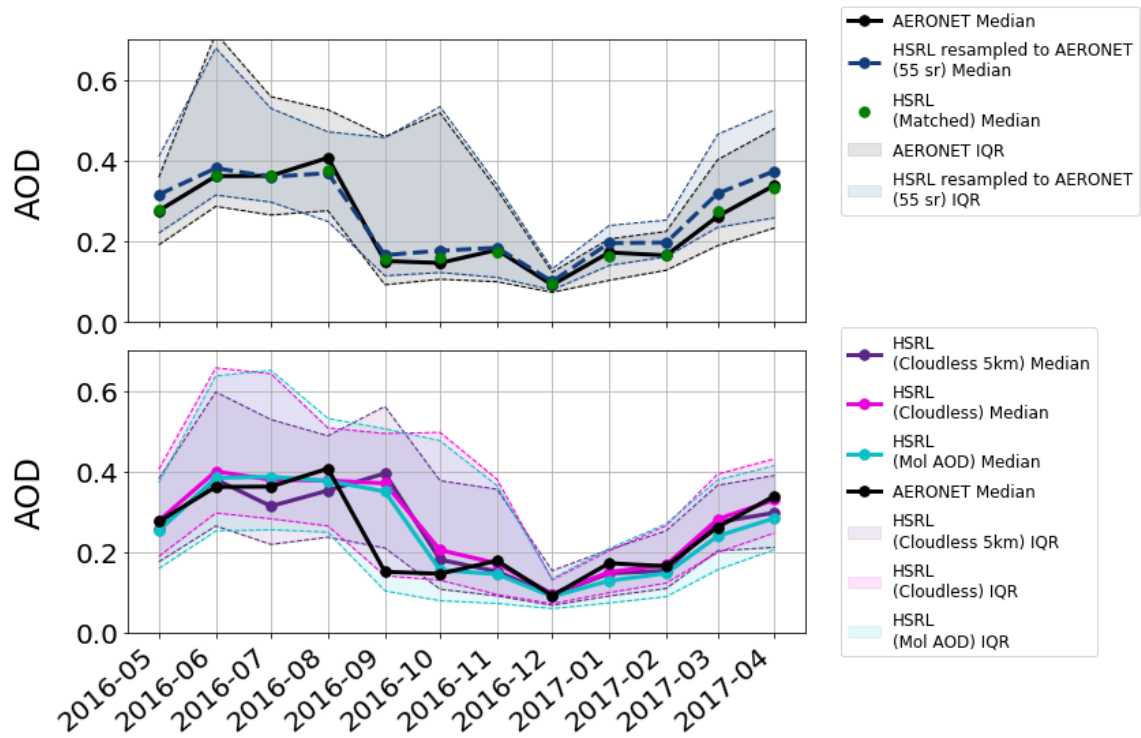


Figure 3.3: Various estimates of monthly-median aerosol optical depth (AOD) in Seoul. Top: All data sampled as AERONET and the effect of lidar ratio is demonstrated by comparing the constant lidar ratio assumption (blue) and interpolated mean lidar ratio (green). Bottom: AERONET AOD and HSRL estimates of AOD. "Cloudless" is defined as having no clouds or virga below the top of integration at 10km. "Cloudless 5km" only integrates to 5km and includes scenes with clouds between 5km and 10km. "Mol. AOD" is the molecular-derived AOD and is sampled the same as "cloudless". All HSRL estimates except "Mol. AOD" assume a bulk lidar ratio interpolated from AERONET-derived monthly means.

In conclusion, AERONET daytime AOD is in good seasonal agreement with all-day AOD from the HSRL. The lack of nighttime observations should cause a high bias in AERONET observations, especially during summer, but does not. Other sources of error include differences in viewing geometry and departures from horizontal homogeneity that could induce disagreement between the AERONET and UW-Madison HSRL.

Diurnal Cycle

In a similar manner to the seasonal cycle, we investigate the diurnal cycle of AOD. Analysis of AERONET-derived AOD as a function of time of day is problematic due to the strong diurnal cycle of cloudiness (AERONET requires clear sky) and AOD.

Figure 3.4 shows the diurnal cycle, as measured by both the HSRL and AERONET. The greatest processing uncertainty originates from the estimation of bulk lidar ratio using AERONET. Only the linearly-interpolated monthly mean lidar ratio is used, so a systematic diurnal cycle in bulk lidar ratio will bias the AOD diurnal cycle. A direct matchup between AERONET and (seasonally-corrected lidar ratio) UW-Madison HSRL AOD (Fig. 3.4 black and green lines) shows very good agreement. The bias is small enough that analysis can continue under the assumption that bulk lidar ratio does not exhibit a significant mean diurnal cycle that might undermine the benefit of superior sampling.

Observed AOD variation during the day is far smaller than seasonal variation, except in summer. There was a significant cycle in the summer months, which has implications for AOD products such as MODIS or CALIOP, which would be observing the near-peak AOD at 1:30pm local time. Figure 3.5 shows just the deviation from daily mean. The mean amplitude is about 0.15 optical depth. This cycle is not completely captured by AERONET due to the reduced sampling, likely a result of cloud cover. Winter also showed a cycle, the amplitude is smaller (~ 0.05), but relative to the mean AOD is about the same. In springtime, the daytime AOD was slightly higher than night (~ 0.05), but the peak occurred earlier than summer or winter, and the amplitude, relative to the mean value, was small in comparison.

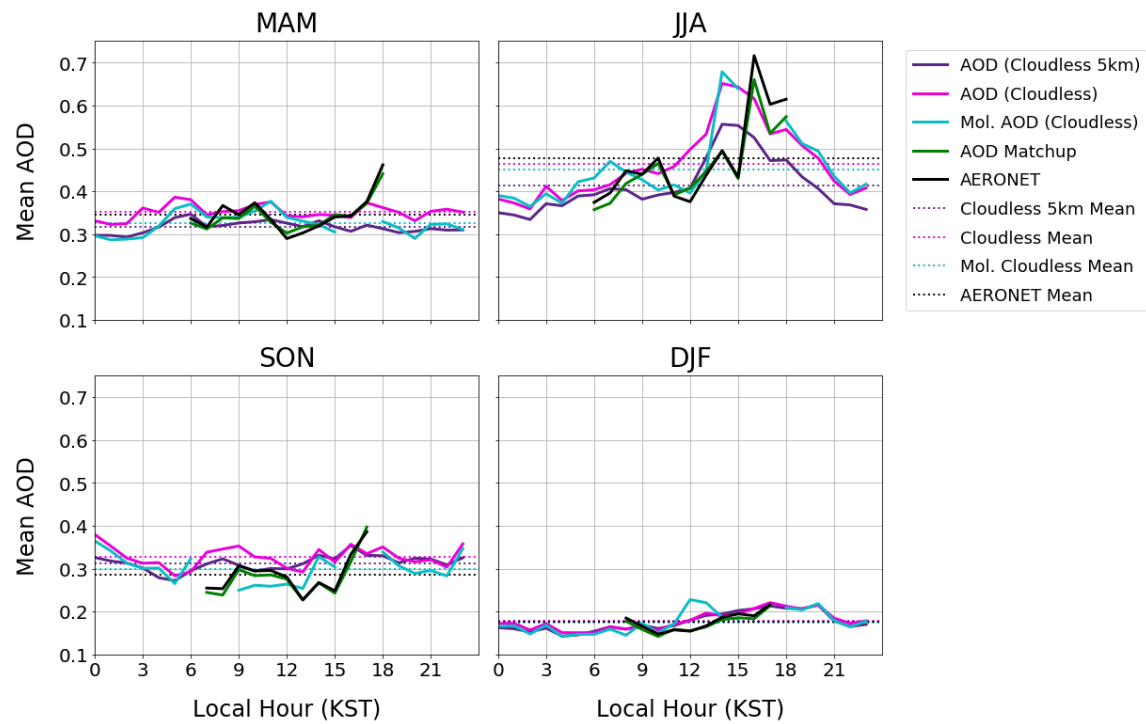


Figure 3.4: AERONET and HSRL AOD estimates aggregated by season and hour-of-day. Descriptions of HSRL various estimates are given in Fig. 3.3. Aggregation excludes hours without adequate representation in each month of the season to prevent some leakage from seasonal AOD trends when sunrise and sunset times co-vary. The seasonal-mean (all inclusive) is plotted as a dotted horizontal line.

In conclusion, the diurnal cycle is negligible in spring and fall, the winter cycle might be important, and the summer cycle is certainly significant. Another conclusion is that the effect of morning rush hour, which has been proposed by others, may be detectable, but is small. Rather than intra-diurnally, the largest variations in AOD remain at the inter-diurnal and seasonal scales. Intuitively, the most significant causal factors of AOD must also fluctuate at these time scales.

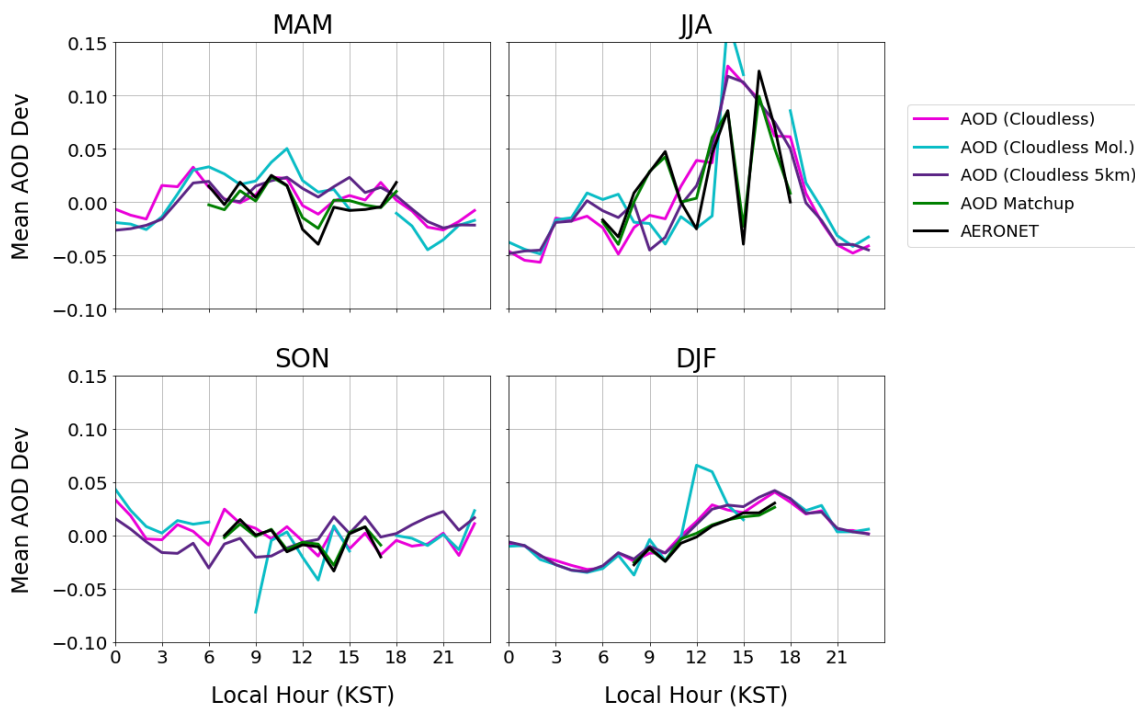


Figure 3.5: Diurnal deviation of AERONET and HSRL AOD estimates aggregated by season and hour-of-day. Similar to Fig 3.4. but daily mean is subtracted.

Weekly cycle

One method to isolate emission effects is to control for the day-of-the-week; the rationale being that day-of-week influences the type of anthropogenic activity independent of meteorological conditions. Several surface studies have documented a weekend effect, which predict elevated concentrations during weekday rush hours. The strength of the effect was found to be quite small for surface PM_{10} concentration in eastern China, only a few $\mu g m^{-3}$ (Gong et al., 2007). However, a study of AOD in Seoul showed a very large weekend effect, with AODs decreasing by 32% during the weekend (Xia et al., 2008). These were able to be reproduced for the time period (not shown). However, analysis of the recent UW-Madison HSRL time period (Fig. 3.6) shows that if there is a weekend effect, it is very small or does not produce differences observable by the UW-Madison HSRL (e.g. only changes

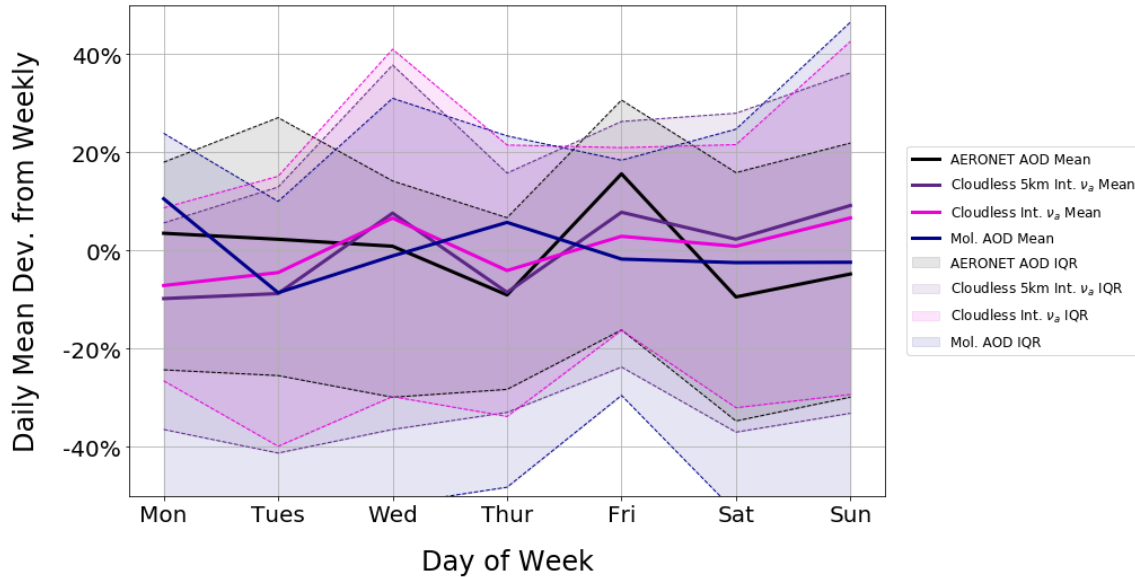


Figure 3.6: Daily mean deviation from weekly mean grouped by day-of-week. Integrated aerosol backscatter coefficient is used for all but one (Molecular AOD) of the HSRL estimates. Interquartile range (IQR) is also plotted to show variance.

chemical apportionment). There may be a slight increasing trend throughout the week, but overall effect is smaller than 10%. The range of deviation on same day between weeks is far larger. Surprisingly, the maximum is reached on Sunday rather than Friday as reported in Xia et al. (2008). The reason for the discrepancy in effect strengths is potentially the decrease in anthropogenic contribution to AOD linked to emissions reductions in the past decade. A long-term downward trend in AOD was noted before in the review, and the studies showing the largest anthropogenic effects were conducted using observations over 10 years old at the time of this analysis. Perhaps the maximum is delayed because now the primary source is foreign and must be transported. Even so, the null hypothesis that the Sunday mean is the same as Monday cannot be rejected with either HSRL or AERONET.

The lack of a large weekend effect is consistent with the lack of a detectable rush hour in the diurnal cycle (Fig. 3.5), as the weekend effect is supposedly mediated by traffic. A vast majority of AOD is anthropogenic and climatological means are

clearly dependent on emissions, but anthropogenic cycles are not manifesting at these timescales. This suggests that either emissions do not fluctuate with great amplitude and/or the responsivity of AOD to emissions is more indirect than expected and non-anthropogenic factors are controlling the most variation. High quality emission inventories could determine the amplitude of fluctuations, but most such inventories do not include weekly cycle information and the formation of particles from gaseous emissions is still uncertain. In the authors opinion, the more plausible hypothesis is that the AOD response to anthropogenic activity is too stochastic to be detected without longer measurement, during which the anthropogenic activity itself may change.

Dust and polarization

As discussed in the review section, dust is detectable by the UW-Madison HSRL because the returns from the irregular-shaped dust particles have high levels of depolarization. The column-integrated HSRL aerosol backscatter coefficient may then be separated into parallel and perpendicular components. Roughly, the perpendicular components isolate some fraction of the backscatter of mineral dust, but very little of organic or secondary inorganic matter.

A dust backscatter retrieval is developed based on this principle and detailed in the methods section. Figure 3.7 validates this retrieval by comparing the integrated dust backscatter coefficient to the coarse-mode optical depth of AERONET, which is often regarded as a proxy for the relatively large dust particles. Figure 3.8 confirms the correlation at the shortest timescales and introduces the seasonal variation in the dust lidar ratio.

The correlation in JJA is much worse than the other seasons, even though the monthly-mean trend is roughly reproduced. Figure 3.9 shows monthly values of dust lidar ratio compared to non-dust and total lidar ratio. The derived dust lidar ratio is a function of assumed dust depolarization and the true dust lidar ratio, and therefore variations indicate changes in one or both. Large variation is somewhat surprising because both lidar ratio and depolarization are expected to

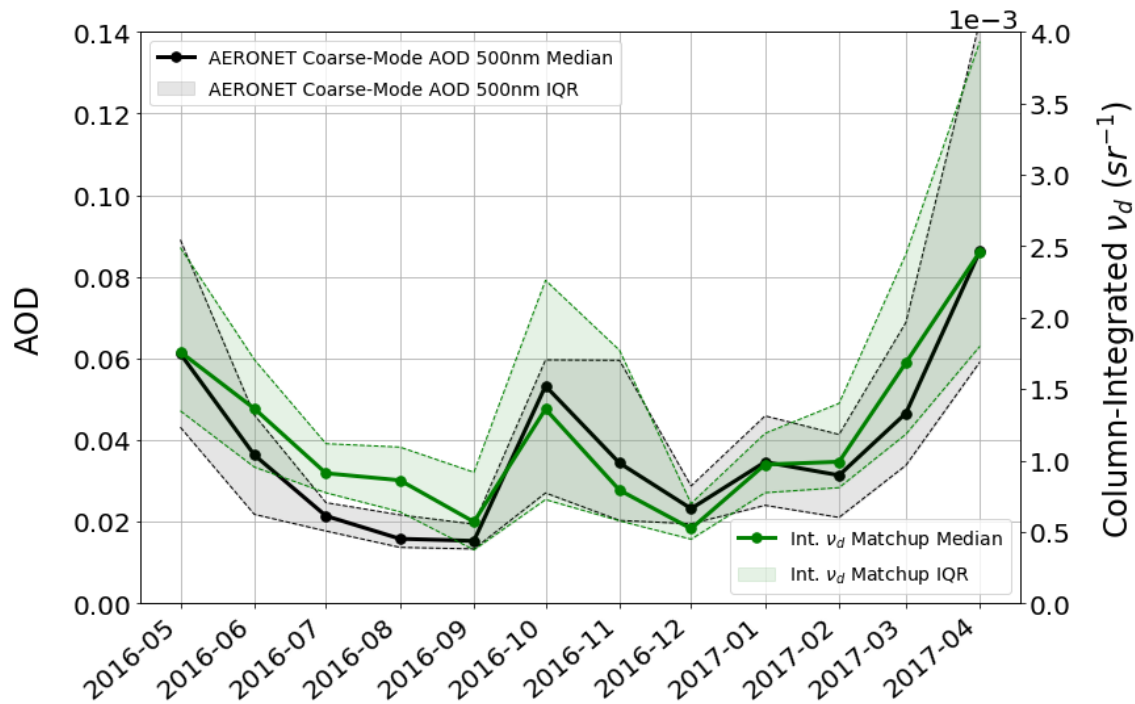


Figure 3.7: Time-series of coarse-mode and dust column optical properties. The black line is monthly-median AERONET coarse-mode AOD. The green line is monthly-median matched dust backscatter integrated up to 10 km. Interquartile range (IQR) is plotted to show variance.

be stable in dust. Coarse-mode non-dust is expected to increase in the summer as the aerosol size-distribution changes. But, this would result in higher coarse-mode AOD as compared to a polarization-based retrieval, not lower as observed. Another possibility is that a greater fraction of dust backscatter is fine mode in the summer, thus it is unaccounted in the AERONET coarse-mode AOD. An alternative source of error is a seasonal bias in the coarse-mode AOD from AERONET.

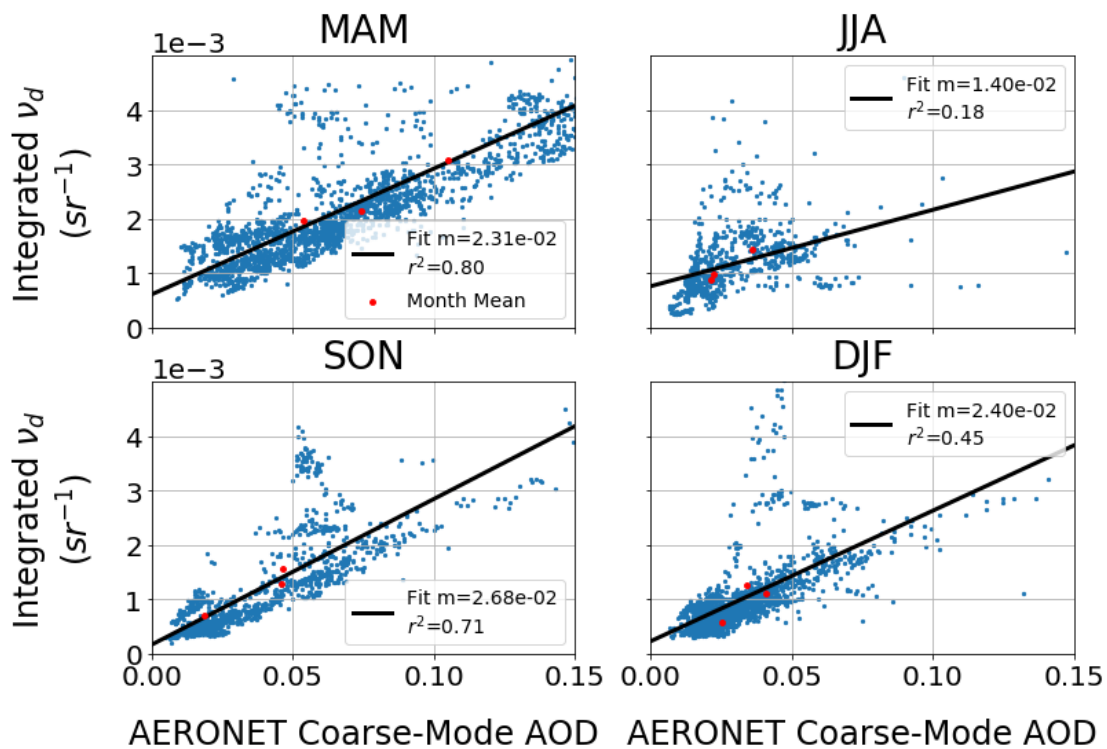


Figure 3.8: Seasonal comparison of coarse-mode AOD and integrated dust backscatter coefficient. Blue dots represent individual matchups between AERONET and HSRL. Red dots show the monthly means for each season. The slope (m) and coefficient of determination (r^2) from linear regression are shown in the legend.

3.1 Vertical Profiles of Backscatter

In analysis involving vertical profiles, the calibrated aerosol backscatter coefficient will be used instead of extinction. Assumption of the lidar ratio profile could allow conversion, but this introduces uncertainty. It could also be estimated by computing the derivative of the logarithmic ratio of the expected and measured molecular signal. However, this process is inherently less sensitive than directly measuring aerosol backscatter, has uncertainty associated with the geometric overlap function, and behaves poorly (sometimes negative or extremely large). Therefore, for

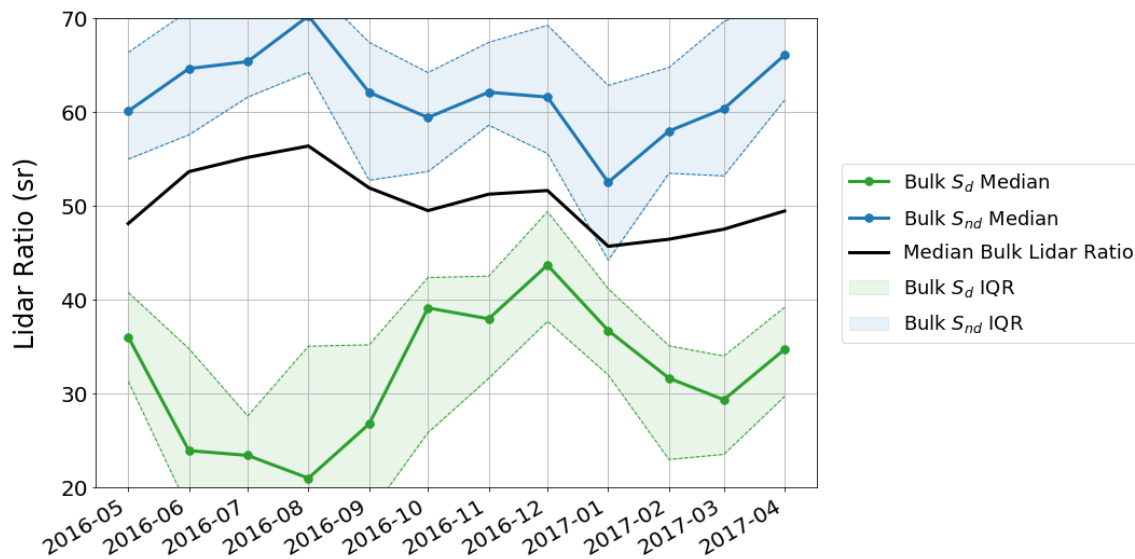


Figure 3.9: Time-series of decomposed bulk lidar ratio. The black line repeats the monthly bulk lidar ratio from Fig. 3.1 (using median instead of mean has little effect). The green line shows the dust bulk lidar ratio (defined as coarse-mode AERONET AOD divided by integrated HSRL dust backscatter). The blue line shows the non-dust bulk lidar ratio (defined as fine-mode AERONET AOD divided by integrated HSRL non-dust backscatter).

questions of aerosol loading it is prudent to first analyze the most defensible proxy measurement, calibrated aerosol backscatter coefficient.

Seasonal Profiles

It has long been known that the average distribution of aerosol mass decreases exponentially with altitude until levelling off above some altitude (Seinfeld and Pandis, 1998). Figure 3.10 shows the vertical distribution of aerosol backscatter coefficient measured by the UW-Madison HSRL in Seoul. Expectations are validated, except within the boundary layer. Below typical boundary layer heights the backscatter profile is not exponential. Especially in the summer median, the curvature is convex near the surface and the decrease with height is slower. This is probably because of higher boundary layers and convective transport of aerosol in

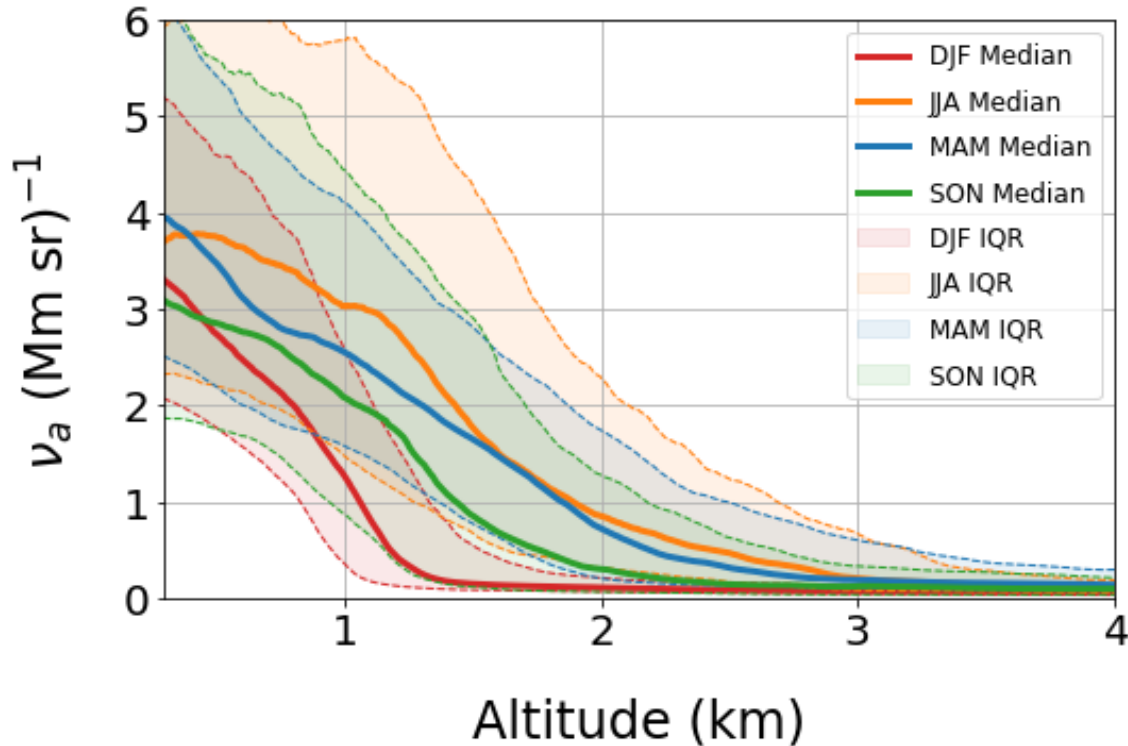


Figure 3.10: Vertical profile of aerosol backscatter coefficient below 4km. The median value and inter-quartile range (IQR) for each season is displayed.

the summer. Another feature is relatively high backscatter in spring above 3 km. Figure 3.11 presents the backscatter above 4 km with the spring profile being most unique. The interquartile range above 4 km is very large and the median value is also high. A likely explanation is lofted dust, which is known to occur during spring.

When showing aggregated profiles, it should be noted that the instantaneous measured backscatter virtually never matches the mean value nor a scaled version of the mean. Usually the appearance is more piecewise, with abundant inversions or plumes at various heights. These non-smooth distributions are not a result of noise or random perturbations as they are temporally coherent on scales of at least hours. The mean distribution only emerges once many days of vertical profiles

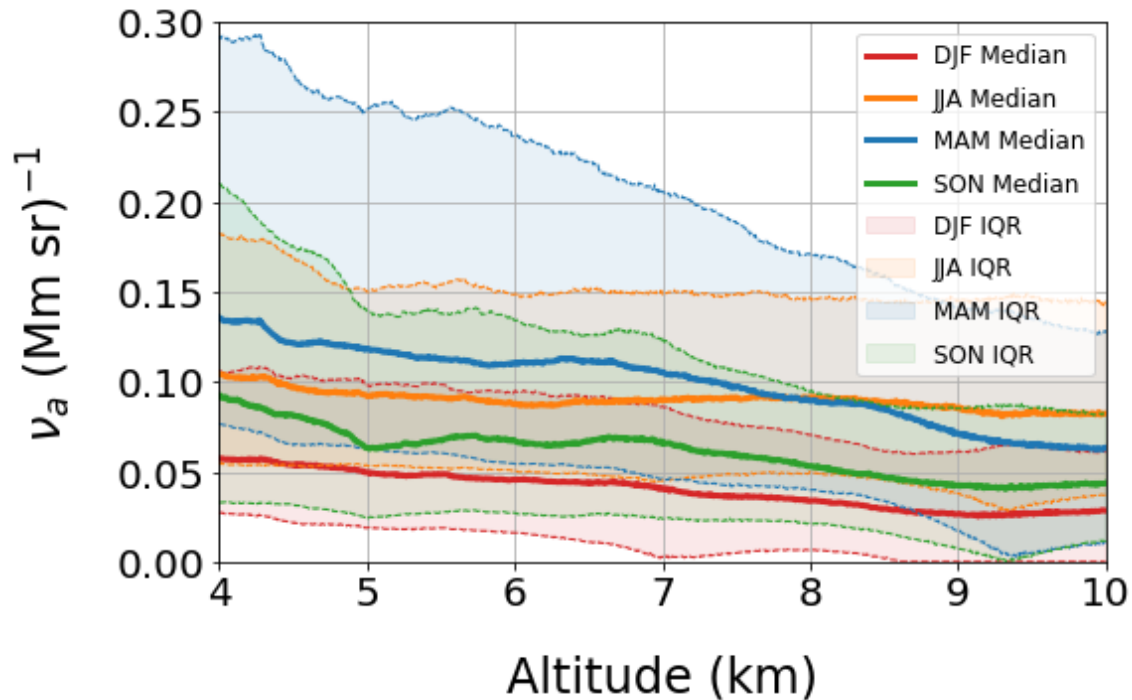


Figure 3.11: Vertical profile of aerosol backscatter coefficient between 4km and 10km. Similar to Fig. 3.10 but at higher altitude and smaller y-scale.

are averaged together. The observed instantaneous distribution is intuitive when the spatial heterogeneity of aerosol sources is considered in combination with vertical shear. Still, to the author's knowledge, little rigorous explanation has been given in the literature about the origin and characteristics of such high entropy vertical profiles. Global or regional aerosol models probably could not produce such diversity in vertical distribution. Large eddy simulations (LES) would likely need to be conducted to answer these questions.

Dust and Polarization

The presence of dust can be detected quite accurately with the UW-Madison HSRL using the polarization of the backscattered returns. An explanation and further

details of dust optical properties were discussed in the review section. Evidence of good performance was shown in the dust section and Figure 3.8. The assumed correspondence between coarse-mode AOD and integrated dust backscatter coefficient can be expanded into the vertical dimension. It is not necessarily true that the lidar ratio will remain constant in the vertical, but because dust is hydrophobic and naturally emitted, the size, shape, and composition is expected to be more stable than other particulates. Figure 3.12 shows the median vertical distribution of dust backscatter coefficient alongside the total aerosol backscatter coefficient for each season.

Increasing aerosol depolarization with altitude was typical in this dataset; however, there are many possible explanations for such a tendency. By decomposing backscatter into dust and non-dust (as in Fig. 3.12), the gradient in depolarization can be attributed to differing vertical distributions of these components. Note that both components decrease with altitude; the majority of backscatter is still located near the surface in each case. However, a persistent difference between the dust and non-dust vertical distribution is a slower decrease in median dust backscatter with altitude. This can be quantified by comparing the fraction of total backscatter attributable to dust, as is done by the green dashed line in Figure 3.12. Near the surface, dust comprises a small fraction of total backscatter, but in the free troposphere it is responsible for about half. One possible explanation is that the backscatter of hygroscopic non-dust is enhanced at low altitudes preferentially to the hydrophobic dust. This can be corrected in non-dust using the hygroscopicity relationship from Figure 3.16, yet the feature remains (green line). Approaching the tropopause, the dust fraction decreases once again. Though, the cross-polarized signal at such high altitudes may be approaching the detection floor of the current averaging scheme, which is a source of error.

Figure 3.13 shows that the NAAPS aerosol model also contains this feature when comparing the vertical distribution of dust extinction, and this increases confidence that dust is indeed responsible and not another type of particle. As far as the author knows, this has not been documented before in the literature. It should be noted that these mean vertical distributions are not at all representative

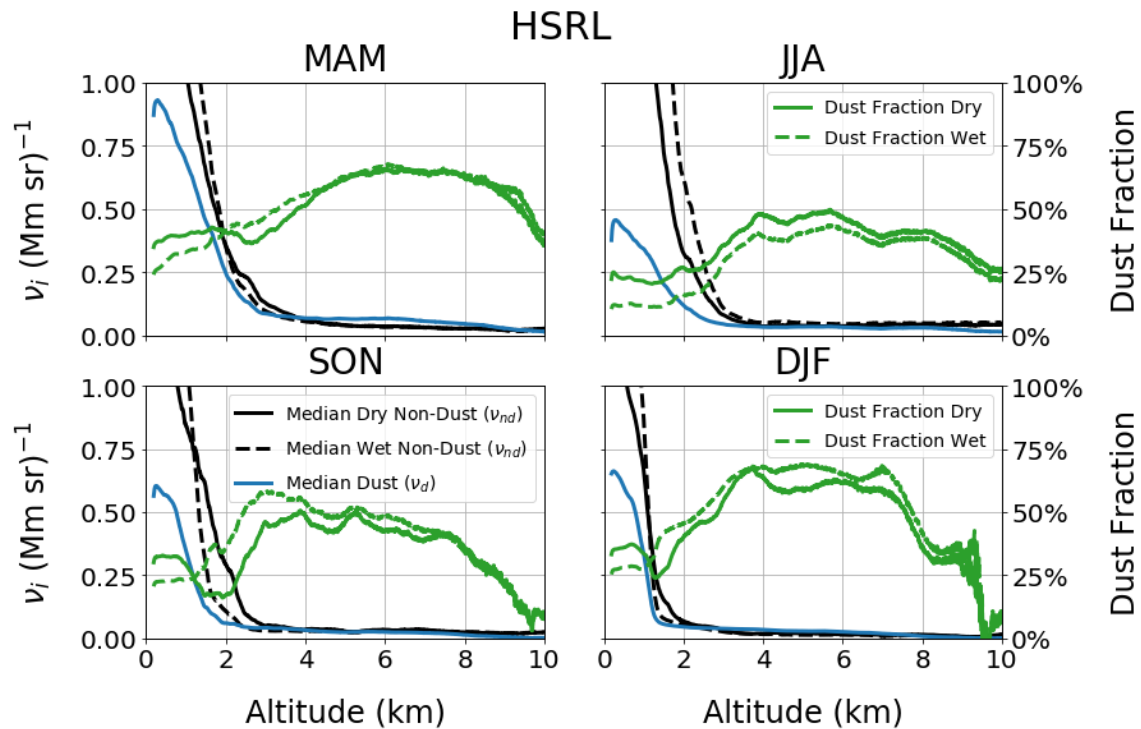


Figure 3.12: Seasonal-mean vertical profiles of dust and non-dust backscatter coefficient and dust fraction at 7.5m vertical resolution. The dashed black line shows seasonal-mean non-dust backscatter coefficient (v_{nd}). The solid black line has been corrected for hygroscopic growth. The blue line shows dust backscatter coefficient (v_d). The dashed green line shows the ratio of median dust to median aerosol backscatter coefficient ($\frac{v_d}{v_{nd}+v_d}$). The solid green line is the same ratio, but using the corrected non-dust backscatter coefficient (dashed black line).

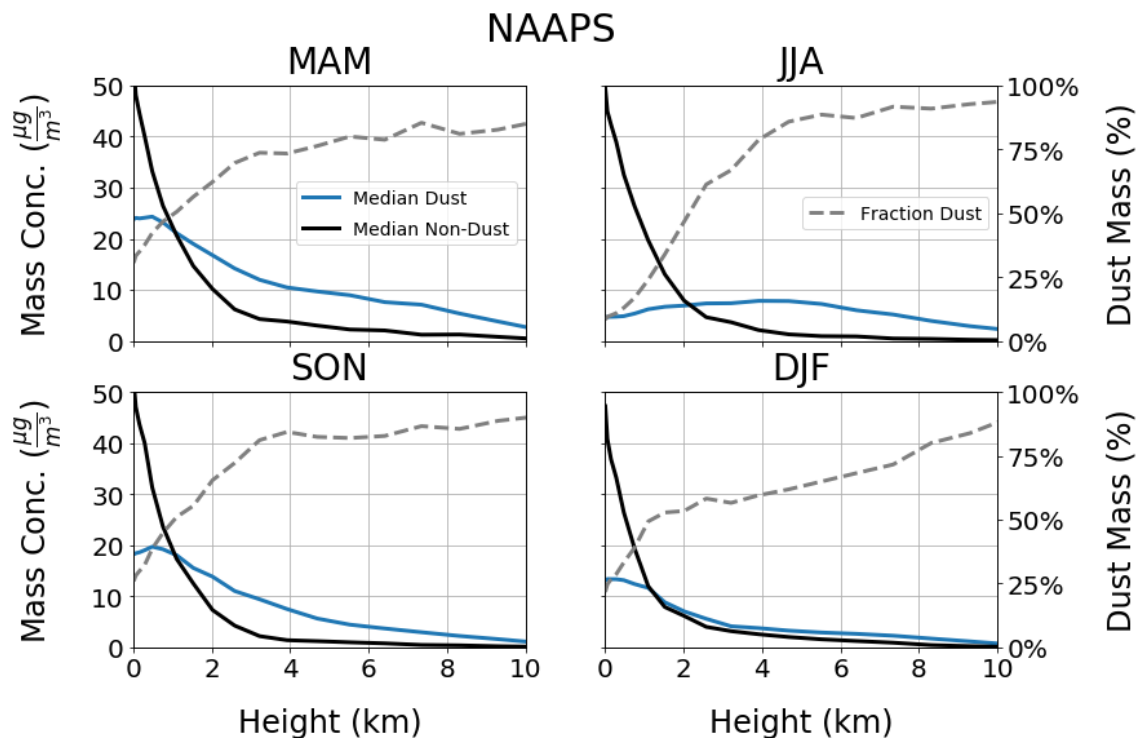


Figure 3.13: Seasonal-mean vertical profiles of dust and non-dust mass concentration from NAAPS aerosol model. The black line shows the non-dust mass concentration. The blue line shows dust mass concentration. The dashed gray line shows the median dust fraction of median total mass concentration.

of a likely instantaneous observation. The mean value is instead averaging across coherent plumes, which complicates the analysis.

Typical dust source regions in the Tarim Basin and Gobi Desert are several days of atmospheric transport away from the UW-Madison HSRL in Seoul, whereas the anthropogenic non-dust species is likely less than a day old before it is advected away. So, one possible explanation is that additional transport time modifies vertical distribution through either vertical transport or preferential removal. Another possibility is that dust from the high-altitude deserts is injected higher into the atmosphere, on average than non-dust, and this raises the center-of-mass. The cause might be best understood through modeling studies since it appears that

this feature is already represented. A potential source of error is that the mean depolarization of the dust is changing in the vertical, specifically in the upper troposphere.

3.2 Vertical Profile of Lidar Ratio

There is great interest in lidar ratio vertical profiles because they can help aerosol type identification and they are needed to retrieve both backscatter and extinction for single-channel lidars (e.g. CALIOP). Figure 3.14 shows profiles of median lidar ratio from the corrected-molecular UW-Madison HSRL and the NASA HSRL2 that was deployed on a DC-8 aircraft during KORUS-AQ (May 2016). The airborne HSRL2 is able to observe much of the atmosphere from a significant distance, which permits more accurate extinction retrievals because the geometric overlap function is better defined. However, the DC-8 was often very far from Seoul which raises questions about how representative the median value might be. Also, the DC-8 flights were only conducted for a relatively short amount of time within a single season. The median lidar ratios from the UW-Madison HSRL are also uncertain because of the uncertain geometric overlap. Corrections were performed as described in methods.

Both lidars agree that lidar ratio is generally higher at the surface and decreases quite dramatically in the transition region from the boundary layer to the free troposphere. Within the free troposphere, the NASA HSRL2 observed nearly constant lidar ratio (~ 30 sr) with altitude. The UW-Madison shows more variation and an even lower lidar ratio (~ 15 sr). Both values are below the typical ranges associated with dust or continental aerosol. The lidar ratios below 30 sr measured by the UW-Madison HSRL are likely in error because of the uncertainty in the geometric overlap function is insufficiently corrected. Nevertheless, the general consensus trend does seem plausible. As demonstrated in Figure 3.2, the higher relative humidity in the boundary layer could cause the higher lidar ratios. Another reason might be the aerosol species; dust typically has a lower lidar ratio than anthropogenic aerosol (also demonstrated in Fig. 3.9), and is a greater fraction of

total scattering and mass in the free troposphere than within the boundary layer (see Fig. 3.12 and 3.13).

The altitude-resolved lidar ratio is also compared to the bulk lidar ratio. The mean bulk lidar ratio is quite close to the boundary layer values, which is to be expected. The bulk lidar ratio inherently weights the aerosol near the surface more because both extinctions and aerosol backscatter coefficients are generally larger. Thin aerosol contributes less to the bulk lidar ratio. Therefore, the variations in bulk lidar ratio are likely to be caused predominantly by changes in boundary layer aerosol properties.

3.3 Surface

Correlation with Backscatter

Figure 3.15 compares the near-surface aerosol backscatter coefficient to surface $PM_{2.5}$ mass concentration. There are several reasons for disagreement. Most importantly, the UW-Madison HSRL will be sensitive to particles larger than 2.5 microns. Secondly, $PM_{2.5}$ is a dry concentration, any hygroscopic growth or water uptake will increase the backscatter relative to the dry concentration. Finally, backscatter is only an optical property. It is proportional to the cross-section, not the volume, and cannot represent variations in density. Differences in aerosol backscatter efficiency caused by material composition will also cause disagreement. That said, the agreement between the two is sufficient to make surface backscatter an acceptable proxy. The bulk approximation is shown in Equation 3.1. where $f(\text{RH})$ is the hygroscopic growth factor and α_{back} is the mass scattering in units $[\text{m}^2/(\text{gsr})]$. Notably, mass scattering is related by the lidar ratio to mass extinction, which is required in aerosol models for AOD assimilation and radiative transfer. The ratio of $PM_{2.5}$ to backscatter changes seasonally as expected, either due to hygroscopic growth or changes to mass backscattering coefficient. The section on lidar ratio established that monthly to seasonal variation in bulk lidar ratio is relatively small, compared to internal variation. Therefore, the most probable explanation is hygro-

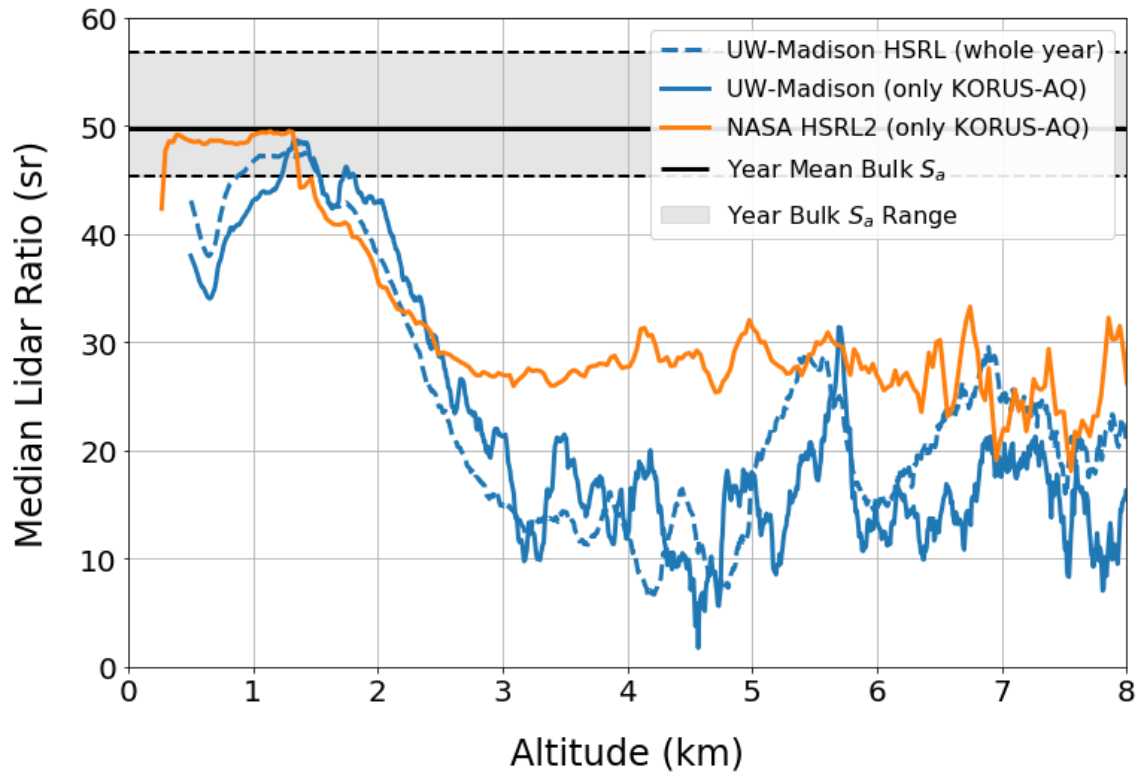


Figure 3.14: Vertical profile of median lidar ratio. In orange, KORUS-AQ data from airborne NASA HSRL2 included for comparison. The UW-Madison HSRL mean for the entire year is shown in dashed blue. The UW-Madison HSRL mean from the same time period as the NASA HSRL2 is also displayed as a solid blue line. The minimum, maximum, and mean monthly-mean bulk lidar ratio (time-series in Fig. 3.1) is also plotted as a black line and filled interval.

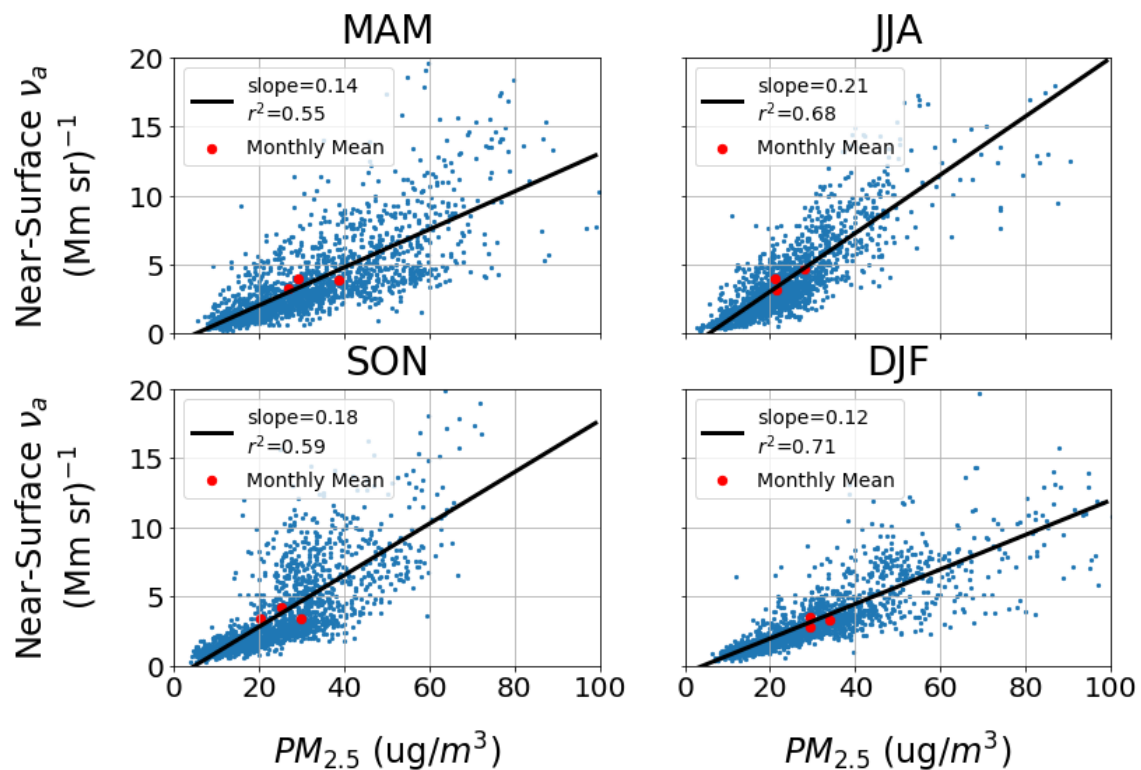


Figure 3.15: Seasonal comparison of near-surface aerosol backscatter coefficient and $PM_{2.5}$. Blue dots are matchups between hourly $PM_{2.5}$ and the backscatter observation that is nearest in time. Red dots are monthly averages of $PM_{2.5}$ and backscatter. Linear regression results (line slope and coefficient of determination) are displayed in legend.

scopic growth. This logic is quantified by a model including near-surface relative humidity from reanalysis data or surface data. The relationship between relative humidity and mass scattering is shown in Figure 3.16. Backscattering efficiency increases nonlinearly with relative humidity as expected. The range of relative humidity in each season clearly determines the mean mass backscattering coefficient. The seasonal linear coefficients of lidar ratio from that figure are also included to show an estimation of mass extinction. Because lidar ratio is thought to increase with relative humidity, aerosol backscatter is actually less sensitive to hygroscopic

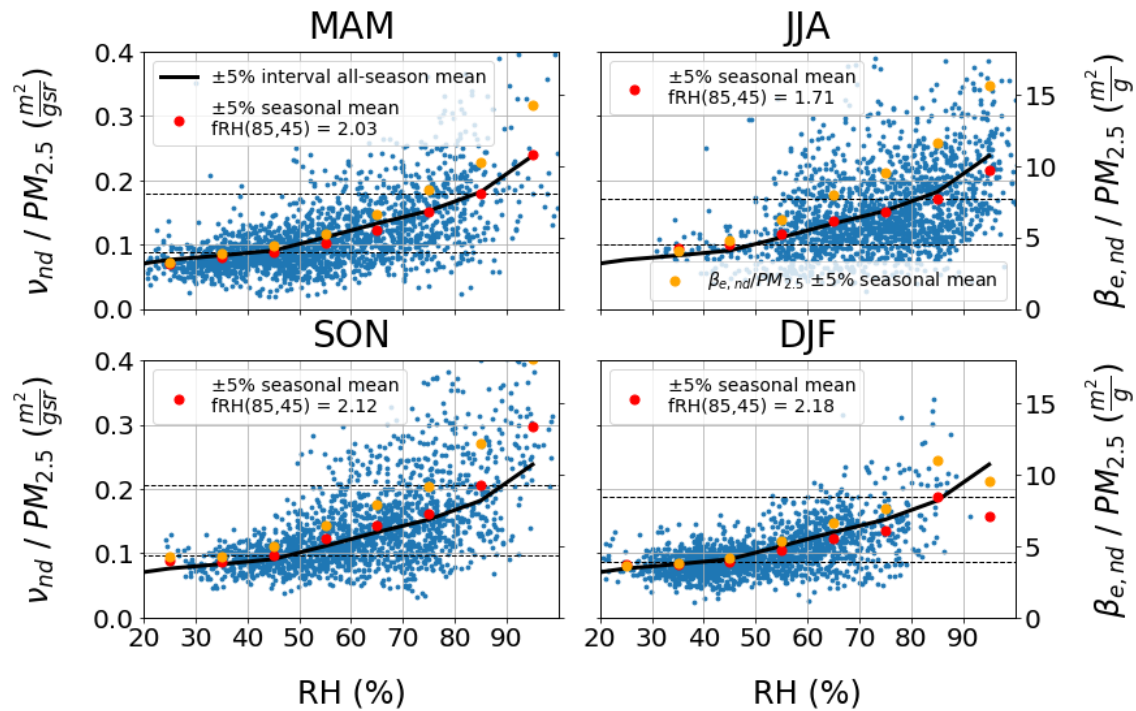


Figure 3.16: Seasonal comparison of surface relative-humidity (RH) and ratio of non-dust backscatter coefficient to $PM_{2.5}$. Blue dots represent matchups between hourly $PM_{2.5}$ observations and the HSRL backscatter nearest in time. Seasonal means binned by RH are computed and displayed in red. The annual mean binned by RH is repeated in each season as a solid black line. The ratio of 85% and 45% is computed and shown in legend and horizontal dashed black lines highlight the values used. Estimated extinction ratio ($\sigma_{s,nd}/PM_{2.5}$) is displayed in orange to show that the probable dependence of lidar ratio on relative humidity would strengthen the effect.

growth than extinction. Unexpectedly, we see little difference between the overall and seasonal hygroscopicity, the curve for each season is close to the annual mean. Known compositional differences between seasons were expected to create large biases. That said, some disagreement (perhaps spurious) occurs at the ends of the relative humidity scale where data is sparse for most seasons. An extinction-based hygroscopicity of ~ 3 between 45% and 85% relative humidity can be calculated using this method. This is quite high; Anderson et al. (2003) found a fine-mode value of about 1.6 for 40%-80% during ACE-Asia.

$$\nu_{nd} = \alpha_{back} Cf(RH) \quad (3.1)$$

Sources of error include: influence from particles larger than 2.5 microns, compositional differences, and errors in reanalysis relative humidity.

In summary, $PM_{2.5}$ can be approximated using UW-Madison HSRL aerosol backscatter coefficient as long as hygroscopic growth can be corrected. The primary implication is that using backscatter as a $PM_{2.5}$ proxy may be appropriate aloft because it is acceptable at the surface. Figure 3.17 shows the monthly $PM_{2.5}$ estimated by the RH-corrected UW-Madison HSRL backscatter. The correction uses the annual mean backscatter hygroscopicity curve from Figure 3.16 which removes most of the seasonal bias. The residual error is quite good ($\leq 6 \mu g m^{-3}$) considering that size filtering does not occur in the lidar estimate as it does in the $PM_{2.5}$ observation.

Column aerosol mass

The backscatter-derived $PM_{2.5}$ approximation can be extended into the vertical so long as relative humidity can be accurately tracked and the bulk approximation holds aloft as at the surface. Fortunately, the usually dryer profiles of clear sky scenes are within the low error regime of the hygroscopicity curve derived previously. Also, it was shown earlier that aerosol backscatter coefficient is less sensitive to hygroscopic growth than extinction because lidar ratio increases with relative humidity, so it should compensate for some inaccuracy in relative humidity. After

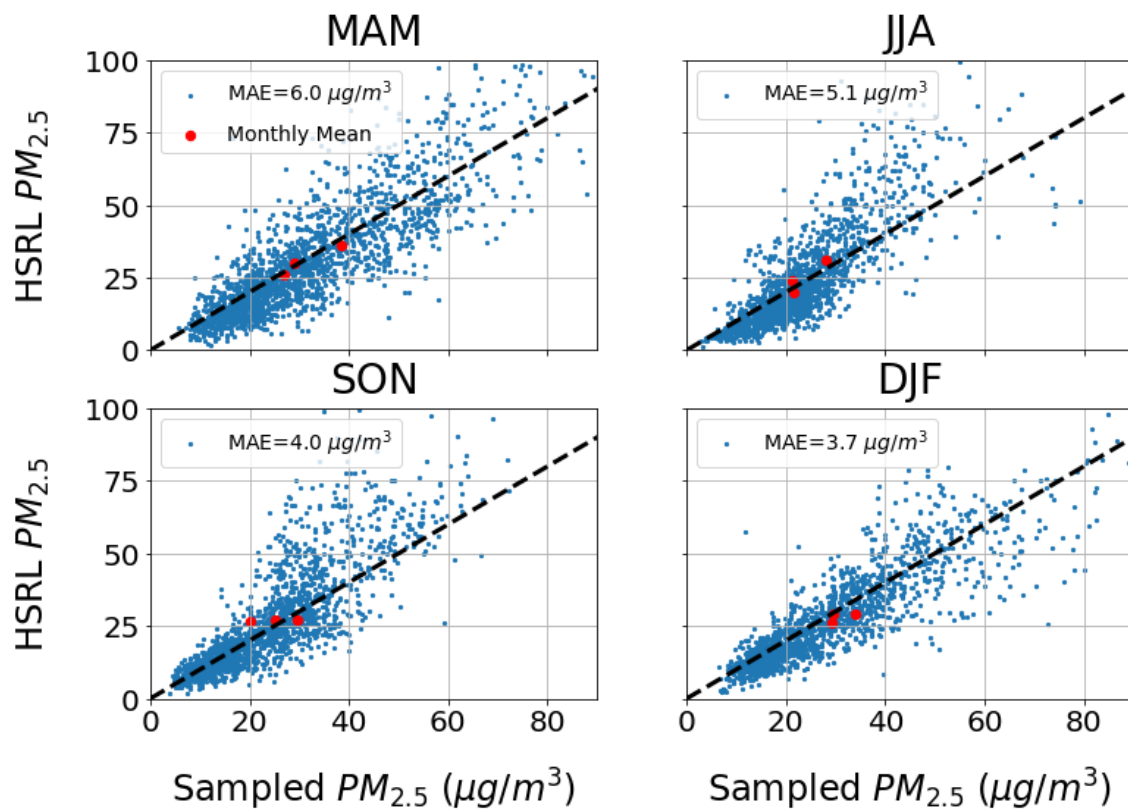


Figure 3.17: Seasonal comparison of HSRL-estimated $PM_{2.5}$ and observed $PM_{2.5}$. Blue dots represent matchups between hourly observed $PM_{2.5}$ and HSRL backscatter nearest in time. Red dots show the monthly mean in each season. The median absolute error (MAE) is computed and displayed in the legend of each season.

the mass profile is estimated, the profile can be integrated to compute the total aerosol mass of a column. The purpose is to determine another column measure of aerosol loading like AOD but more decoupled from meteorology, independent of hygroscopic growth effects.

Figure 3.18 compares the UW-Madison HSRL-derived column dry mass and the column dry mass from the NAAPS aerosol model. The seasonality is different from both the AOD and $PM_{2.5}$ seasonality shown before, but the model and observations roughly agree in both magnitude and seasonality. The main influences on column

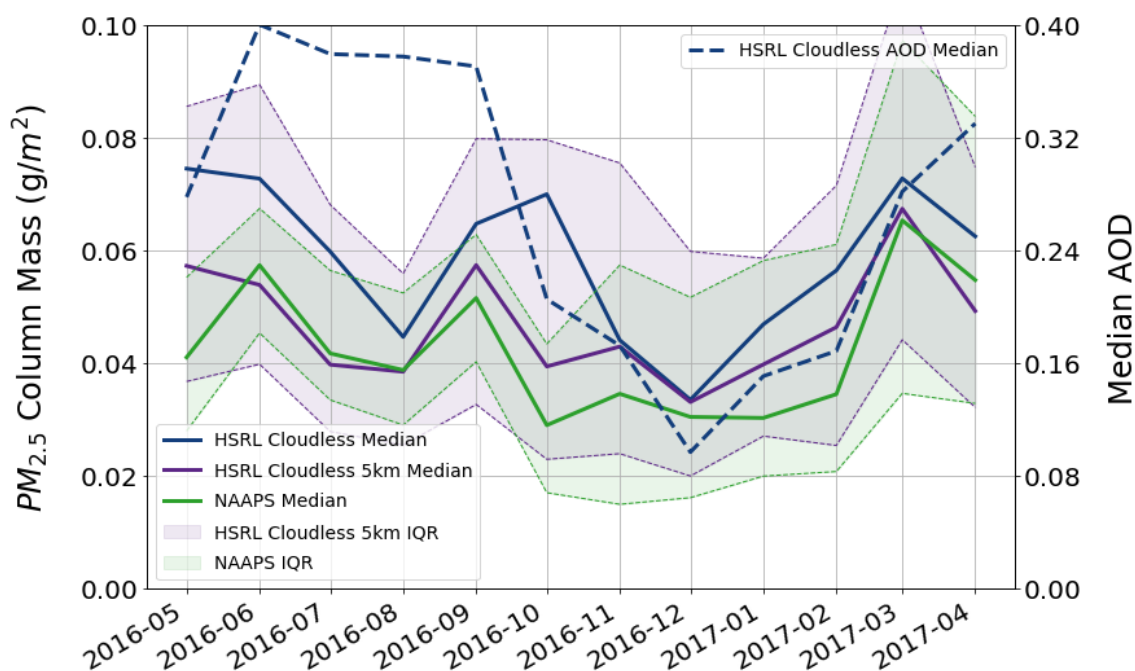


Figure 3.18: Time-series of median column dry fine-mode mass (integrated $PM_{2.5}$). The green line is NAAPS aerosol model fine-mode integrated mass concentration which outputs at 6-hour time resolution. The blue line is the HSRL-derived column fine-mode mass up to 10km from the cloudless subset. The purple line is the HSRL-derived column fine-mode mass (up to 5km) from the "cloudless 5km" subset. Interquartile range (IQR) is plotted to show variance. Derivation of mass is detailed in methods. The median HSRL-derived AOD from "cloudless" subset is plotted as a dashed line for comparison.

mass are advection and divergence related to sources and sinks of aerosol in the volume of atmosphere above Seoul. During the southwest monsoon rainy season, it is clear that PM mass decreases in July and August, contrary to AOD seasonality. A rebound occurs in September. In late fall and winter, mean PM column mass is smallest and remains mostly constant. The highest mean mass occurs in June and March. The observations and model agree on these features.

Changes in the size distribution unrelated to hygroscopic growth could conceivably cause biases through changing the mass backscattering coefficient, which

is not included in our retrieval model. The NAAPS model only has a single size bin for each species and assimilates MODIS AODs, so it could also include these identical biases (Lynch et al., 2016). Comparison with a simulation that models size distribution is left as potential future work.

Dust and Polarization

Asian dust is primarily coarse-mode (Anderson et al., 2003). Therefore, $PM_{2.5}$ is not sensitive to dust and elucidation of its hygroscopic properties is more difficult than the previously-treated dominant fine-mode. Figure 3.19 shows a strong negative correlation between near-surface dust fraction and surface relative humidity. The analysis is limited to the surface for two reasons. First, it has already been demonstrated that dust-fraction increases with altitude. It can be assumed that the relative humidity also decreases with altitude as the air becomes more rarified; this means there is already a non-causal correlation. The second reason is that the surface should have the most accurate relative humidity from the reanalysis. At the surface, the decrease in dust fraction with increases in relative humidity can be explained by hygroscopic growth of spherical low-depolarization particles, meanwhile hydrophobic high-depolarization dust does not grow. This must be true to justify the treatment of dust as hydrophobic in the creation of Figure 3.12.

To strengthen this theory, the non-dust backscatter (Fig. 3.20) shows that the range of aerosol backscatter coefficient itself increases with relative humidity, as expected. This was already demonstrated somewhat with Figure 3.16, but the mass concentration could be controlled for. Figure 3.20 shows that non-dust backscatter coefficient tends to increase at high relative humidity even when marginalizing concentration, which is captured by the figure as variance is more extreme there. The dust backscatter coefficient in Figure 3.21 is submitted as the final evidence needed. As expected, the correlation with relative humidity disappears, owing to the fact that the dominant scatterer is hydrophobic dust. All of these relationships are seasonally robust.

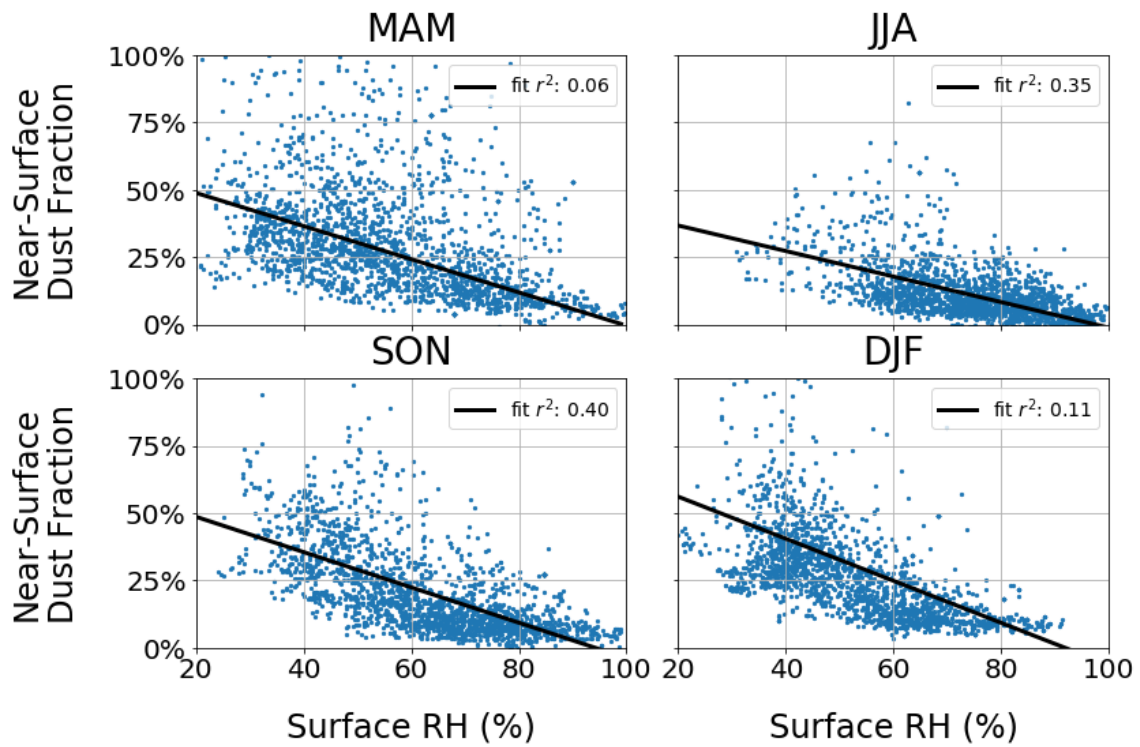


Figure 3.19: Seasonal comparison of near-surface aerosol backscatter coefficient dust fraction and surface relative humidity. Blue dots show hourly relative humidity from ERA5 and the matched HSRL aerosol backscatter coefficient dust fraction nearest in time. Both are sampled near the surface. Coefficient of determination (r^2) from linear regression is shown in the legend.

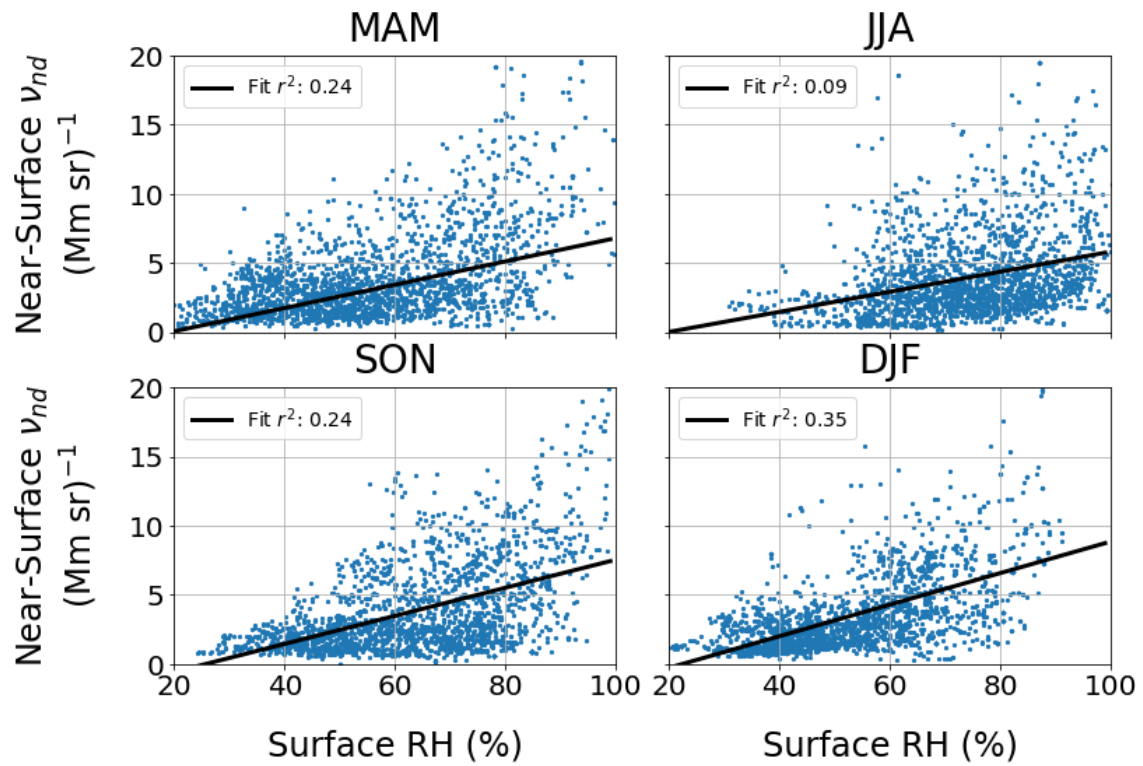


Figure 3.20: Seasonal comparison of near-surface non-dust backscatter coefficient and surface relative humidity. Figure details similar to Fig. 3.19.

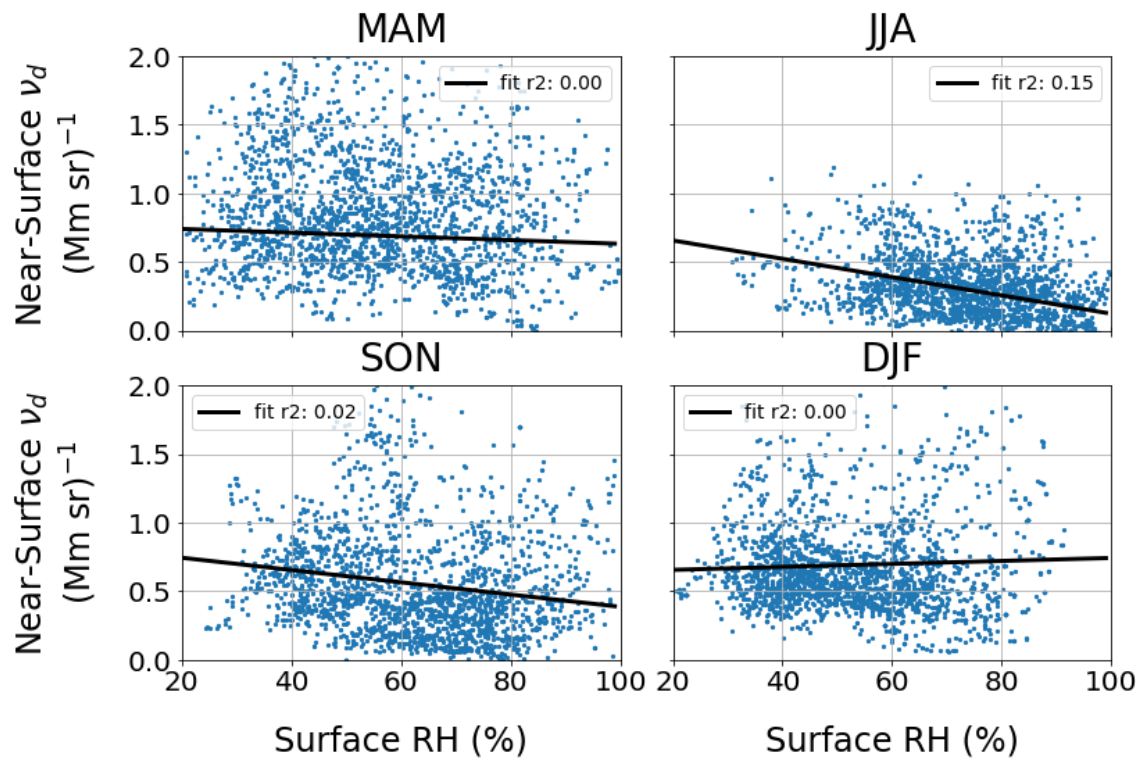


Figure 3.21: Seasonal comparison of near-surface dust backscatter coefficient and surface relative humidity. Figure details similar to Fig. 3.19.

4 CONCLUSION

In this thesis, one year of data from the UW-Madison HSRL located in Seoul during the KORUS-AQ field campaign was processed and analyzed. Rather than choosing a single topic to scrutinize in-depth, these analyses broadly covered a number of different science questions. For each thread, the process was similar. First, an existing measurement was identified. Next, a process was designed to make the UW-Madison HSRL data comparable, and the transformation was validated. Finally, the unique advantages of the HSRL were exploited to extend this process to previously unobserved territory. This procedure was repeated for AERONET AOD, AERONET SDA, and surface $PM_{2.5}$.

The AOD from AERONET is widely-used and is generally well-regarded. Using the UW-Madison HSRL, two fundamentally different methods were used to successfully estimate aerosol optical depth. Then, the superior sampling of the UW-Madison HSRL was used to characterize seasonal, diurnal, and weekly cycle. These results improved on the original AERONET results tremendously with fewer spurious variations and more complete coverage. The effect is enough to qualitatively change the diurnal cycle in some cases.

The AERONET SDA allows AOD to be decomposed into coarse and fine-mode components. Considering the established properties of aerosol in East Asia, coarse-mode was assumed to be dominated by dust. A decomposition of backscatter into dust and non-dust components was designed for lidar data and validated against the coarse-mode AOD. Then, the decomposition could be extended to vertically disaggregated lidar data. The resulting vertical profiles of dust and non-dust help explain the phenomenon of increasing aerosol depolarization with altitude.

Finally, surface measurements of $PM_{2.5}$ were estimated using the near-surface backscatter measurements from the UW-Madison HSRL. A $PM_{2.5}$ retrieval, with correction for hygroscopic growth, was designed and validated. Then, the retrieval was applied along an atmospheric column to produce the column mass. The column mass is interpreted to be similar to AOD, with the advantage of having

less dependence on the hygroscopic growth. Comparison of column mass and AOD seasonality were shown to have qualitative differences, likely due to large influences of meteorology on AOD.

A key result of this thesis is the strong influence of meteorology, particularly relative humidity, on the optical properties of aerosols in Seoul. This finding is likely to generalize to other locations, and therefore it is important to secure accurate and high resolution relative humidity information for the troposphere. Calculation of monthly column mass can only be defended because reanalysis relative humidity is assumed unbiased and the implicit correlation between PM and RH is also assumed to be unbiased. For higher resolution or vertical profiles, the reanalysis is untrustworthy and assimilated radiosonde launches lack the temporal resolution needed. Instead, retrieved moisture profiles from colocated infrared or microwave remote sensing instruments would be ideal.

REFERENCES

- Ackermann, Jörg. 1998. The Extinction-to-Backscatter Ratio of Tropospheric Aerosol: A Numerical Study. *Journal of Atmospheric and Oceanic Technology* 15(4): 1043–1050. 00323.
- Ahmed, Ezaz, Ki-Hyun Kim, Zang-Ho Shon, and Sang-Keun Song. 2015. Long-term trend of airborne particulate matter in Seoul, Korea from 2004 to 2013. *Atmospheric Environment* 101:125–133. 00027.
- Anderson, Theodore L., Sarah J. Masonis, David S. Covert, Norman C. Ahlquist, Steven G. Howell, Antony D. Clarke, and Cameron S. McNaughton. 2003. Variability of aerosol optical properties derived from in situ aircraft measurements during ACE-Asia. *Journal of Geophysical Research: Atmospheres* 108(D23). 00211.
- Ansmann, A., M. Riebesell, U. Wandinger, C. Weitkamp, E. Voss, W. Lahmann, and W. Michaelis. 1992. Combined raman elastic-backscatter LIDAR for vertical profiling of moisture, aerosol extinction, backscatter, and LIDAR ratio. *Applied Physics B* 55(1):18–28. 00438.
- Barnaba, Francesca, and Gian Paolo Gobbi. 2001. Lidar estimation of tropospheric aerosol extinction, surface area and volume: Maritime and desert-dust cases. *Journal of Geophysical Research: Atmospheres* 106(D3):3005–3018.
- Buzorius, G., C. S. McNaughton, A. D. Clarke, D. S. Covert, B. Blomquist, K. Nielsen, and F. J. Brechtel. 2004. Secondary aerosol formation in continental outflow conditions during ACE-Asia. *Journal of Geophysical Research: Atmospheres* 109(D24). 00000.
- C3S, Copernicus Climate Change Service. 2017. ERA5: Fifth generation of ECMWF atmospheric reanalyses of the global climate. 00000.
- Chan, Chak K., and Xiaohong Yao. 2008. Air pollution in mega cities in China. *Atmospheric Environment* 42(1):1–42.

Chang, C.-P., ed. 2004. *East Asian monsoon*. World Scientific series on meteorology of East Asia v. 2, Hackensack, NJ: World Scientific. 00170 OCLC: ocm57343331.

Choi, Jong-kyu, Jong-Bae Heo, Soo-Jin Ban, Seung-Muk Yi, and Kyung-Duk Zoh. 2013. Source apportionment of PM_{2.5} at the coastal area in Korea. *Science of The Total Environment* 447:370–380. 00053.

Coffey, Helen. 2018. Seoul offers free public transport to combat thick layer of smog. *The Independent*. 00000.

Eck, T. F., B. N. Holben, O. Dubovik, A. Smirnov, P. Goloub, H. B. Chen, B. Chatenet, L. Gomes, X.-Y. Zhang, S.-C. Tsay, Q. Ji, D. Giles, and I. Slutsker. 2005. Columnar aerosol optical properties at AERONET sites in central eastern Asia and aerosol transport to the tropical mid-Pacific. *Journal of Geophysical Research (Atmospheres)* 110:D06202. 00000.

Eck, T. F., B. N. Holben, J. S. Reid, P. Xian, D. M. Giles, A. Sinyuk, A. Smirnov, J. S. Schafer, I. Slutsker, J. Kim, J.-H. Koo, M. Choi, K. C. Kim, I. Sano, A. Arola, A. M. Sayer, R. C. Levy, L. A. Munchak, N. T. O'Neill, A. Lyapustin, N. C. Hsu, C. A. Randles, A. M. Da Silva, V. Buchard, R. C. Govindaraju, E. Hyer, J. H. Crawford, P. Wang, and X. Xia. 2018. Observations of the Interaction and Transport of Fine Mode Aerosols With Cloud and/or Fog in Northeast Asia From Aerosol Robotic Network and Satellite Remote Sensing. *Journal of Geophysical Research: Atmospheres* 123(10):5560–5587. 00012.

Eloranta, Edwin. 2014. High Spectral Resolution lidar measurements of atmospheric extinction: Progress and challenges. In *High Spectral Resolution lidar measurements of atmospheric extinction: Progress and challenges*, 1–6. IEEE.

Fernald, Frederick G., Benjamin M. Herman, and John A. Reagan. 1972. Determination of Aerosol Height Distributions by Lidar. *Journal of Applied Meteorology* 11(3):482–489. 00464.

- Gong, Dao-Yi, Chang-Hoi Ho, Deliang Chen, Yun Qian, Yong-Sang Choi, and Jinwon Kim. 2007. Weekly cycle of aerosol-meteorology interaction over China. *Journal of Geophysical Research: Atmospheres* 112(D22). 00120.
- Grund, Christian J., and Edwin W. Eloranta. 1991. University of Wisconsin High Spectral Resolution Lidar. *Optical Engineering* 30(1):6–13. 00000.
- Harrison, Roy M., and Jianxin Yin. 2000. Particulate matter in the atmosphere: which particle properties are important for its effects on health? *Science of The Total Environment* 249(1):85–101. 01013.
- Heo, J.-B., P. K. Hopke, and S.-M. Yi. 2009. Source apportionment of PM_{2.5} in Seoul, Korea. *Atmospheric Chemistry and Physics* 9(14):4957–4971. 00000.
- Heo, Junghwa, Jin-soo Park, Bong Mann Kim, Sang-woo Kim, Rokjin J. Park, Haeun Jeon, and Soon-chang Yoon. 2017. Two notable features in PM10 data and analysis of their causes. *Air Quality, Atmosphere, & Health; Dordrecht* 10(8):991–998. 00000.
- Holz, Robert E. 2002. Measurements of cirrus backscatter phase functions using a high spectral resolution lidar. PhD Thesis, University of Wisconsin–Madison. 00006.
- Jeong, Jaein I., Rokjin J. Park, Jung-Hun Woo, Young-Ji Han, and Seung-Muk Yi. 2011. Source contributions to carbonaceous aerosol concentrations in Korea. *Atmospheric Environment* 45(5):1116–1125. 00032.
- Jung, Jinsang, Youngsook Lyu, Minhee Lee, Taekyung Hwang, Sangil Lee, and Sanghyub Oh. 2016. Impact of Siberian forest fires on the atmosphere over the Korean Peninsula during summer 2014. *Atmospheric Chemistry and Physics* 16(11): 6757–6770. 00014.
- Kang, Choong-Min, Byung-Wook Kang, and Hak Sung Lee. 2006. Source Identification and Trends in Concentrations of Gaseous and Fine Particulate Principal

Species in Seoul, South Korea. *Journal of the Air & Waste Management Association* 56(7):911–921. 00046.

Kim, Byeong-Uk, Changhan Bae, Hyun Cheol Kim, Eunhye Kim, and Soontae Kim. 2017a. Spatially and chemically resolved source apportionment analysis: Case study of high particulate matter event. *Atmospheric Environment* 162:55–70. 00014.

Kim, Hwajin, Qi Zhang, and Jongbae Heo. 2018a. Influence of intense secondary aerosol formation and long-range transport on aerosol chemistry and properties in the Seoul Metropolitan Area during spring time: results from KORUS-AQ. *Atmospheric Chemistry and Physics* 18(10):7149–7168. 00002.

Kim, Hyun Cheol, Eunhye Kim, Changhan Bae, Jeong Hoon Cho, Byeong-Uk Kim, and Soontae Kim. 2017b. Regional contributions to particulate matter concentration in the Seoul metropolitan area, South Korea: seasonal variation and sensitivity to meteorology and emissions inventory. *Atmospheric Chemistry and Physics* 17(17): 10315–10332. 00016.

Kim, Hyun Cheol, Soontae Kim, Byeong-Uk Kim, Chun-Sil Jin, Songyou Hong, Rokjin Park, Seok-Woo Son, Changhan Bae, MinAh Bae, Chang-Keun Song, and Ariel Stein. 2017c. Recent increase of surface particulate matter concentrations in the Seoul Metropolitan Area, Korea. *Scientific Reports* 7(1):4710. 00014.

Kim, Hyun-Sun, Jong-Bae Huh, Philip K. Hopke, Thomas M. Holsen, and Seung-Muk Yi. 2007a. Characteristics of the major chemical constituents of PM_{2.5} and smog events in Seoul, Korea in 2003 and 2004. *Atmospheric Environment* 41(32): 6762–6770. 00151.

Kim, Jiyoung. 2008. Transport routes and source regions of Asian dust observed in Korea during the past 40 years (1965–2004). *Atmospheric Environment* 42(19): 4778–4789. 00107.

Kim, Jiyoung, Soon-Chang Yoon, Anne Jefferson, and Sang-Woo Kim. 2006. Aerosol hygroscopic properties during Asian dust, pollution, and biomass burning

episodes at Gosan, Korea in April 2001. *Atmospheric Environment* 40(8):1550–1560. 00000.

Kim, Man-Hae, Huidong Yeo, Nobuo Sugimoto, Han-Cheol Lim, Chul-Kyu Lee, Bok-Haeng Heo, Yung-Suk Yu, Byung-Ju Sohn, Soon-Chang Yoon, and Sang-Woo Kim. 2015. Estimation of Particle Mass Concentration from Lidar Measurement'. *Atmosphere-Korea* 25(1):169–177. 00003 WOS:000422579500013.

Kim, Sang-Woo, Soon-Chang Yoon, Jiyoung Kim, and Seung-Yeon Kim. 2007b. Seasonal and monthly variations of columnar aerosol optical properties over east Asia determined from multi-year MODIS, LIDAR, and AERONET Sun/sky radiometer measurements. *Atmospheric Environment* 41(8):1634–1651. 00000.

Kim, Yong Pyo, and Gangwoong Lee. 2018. Trend of Air Quality in Seoul: Policy and Science. *Aerosol and Air Quality Research* 18(9):2141–2156. 00002.

Kim, Yumi, Jihoon Seo, Jin Young Kim, Ji Yi Lee, Hwajin Kim, and Bong Mann Kim. 2018b. Characterization of PM_{2.5} and identification of transported secondary and biomass burning contribution in Seoul, Korea. *Environmental Science and Pollution Research* 25(5):4330–4343. 00000.

Koo, Youn-Seo, Sung-Tae Kim, Hui-Young Yun, Jin-Seok Han, Jung-Young Lee, Ki-Hyun Kim, and Eui-Chan Jeon. 2008. The simulation of aerosol transport over East Asia region. *Atmospheric Research* 90(2):264–271. 00035.

Kuehn, Ralph, Robert Holz, Edwin Eloranta, Mark Vaughan, and Johnathan Hair. 2016. Developing a Climatology of Cirrus Lidar Ratios Using University of Wisconsin HSRL Observations. In *EPJ Web of Conferences; Les Ulis*, vol. 119. Les Ulis, France, Les Ulis: EDP Sciences. 00000.

Lee, Seung-Jae, Juwon Lee, Steven J. Greybush, Minseok Kang, and Joon Kim. 2013. Spatial and Temporal Variation in PBL Height over the Korean Peninsula in the KMA Operational Regional Model. *Advances in Meteorology*. 00009.

- Lennartson, Elizabeth M., Jun Wang, Juping Gu, Lorena Castro Garcia, Cui Ge, Meng Gao, Myungje Choi, Pablo E. Saide, Gregory R. Carmichael, and Jhoon Kim. 2018. Diurnal variation of aerosol optical depth and PM 2.5 in South Korea: a synthesis from AERONET, satellite (GOCI), KORUS-AQ observation, and the WRF-Chem model. *Atmospheric Chemistry and Physics* 18(20):15125–15144. 00002.
- Liu, Zhiquan, Quanhua Liu, Hui-Chuan Lin, Craig S. Schwartz, Yen-Huei Lee, and Tijian Wang. 2011. Three-dimensional variational assimilation of MODIS aerosol optical depth: Implementation and application to a dust storm over East Asia. *Journal of Geophysical Research: Atmospheres* 116(D23). 00000.
- Lynch, P., J. S. Reid, D. L. Westphal, J. Zhang, T. F. Hogan, E. J. Hyer, C. A. Curtis, D. A. Hegg, Y. Shi, J. R. Campbell, J. I. Rubin, W. R. Sessions, F. J. Turk, and A. L. Walker. 2016. An 11-year global gridded aerosol optical thickness reanalysis (v1.0) for atmospheric and climate sciences. *Geosci. Model Dev.* 9(4):1489–1522. 00000.
- Ma, Xiaoyan, Tong Sha, Jianying Wang, Hailing Jia, and Rong Tian. 2018. Investigating impact of emission inventories on PM(2.5)simulations over North China Plain by WRF-Chem. *Atmospheric Environment* 195:125–140. 00000 WOS:000450383000011.
- Ma, Xiaoyan, and Fangqun Yu. 2015. Seasonal and spatial variations of global aerosol optical depth: multi-year modelling with GEOS-Chem-APM and comparisons with multiple-platform observations. *Tellus B: Chemical and Physical Meteorology* 67(1):25115. 00011.
- Mao, Feiyue, Wei Gong, and Jun Li. 2012. Geometrical form factor calculation using Monte Carlo integration for lidar. *Optics & Laser Technology* 44(4):907–912. 00015.
- Mishchenko, Michael I., Larry D. Travis, Ralph A. Kahn, and Robert A. West. 1997. Modeling phase functions for dustlike tropospheric aerosols using a shape mixture of randomly oriented polydisperse spheroids. *Journal of Geophysical Research: Atmospheres* 102(D14):16831–16847. 00000.

- Murayama, Toshiyuki, Nobuo Sugimoto, Itsushi Uno, Kisei Kinoshita, Kazuma Aoki, Naseru Hagiwara, Zhaoyan Liu, Ichiro Matsui, Tetsu Sakai, Takashi Shibata, Kimio Arao, Byung-Ju Sohn, Jae-Gwang Won, Soon-Chang Yoon, Tao Li, Jun Zhou, Huanling Hu, Makoto Abo, Kengo Iokibe, Ryuji Koga, and Yasunobu Iwasaka. 2001. Ground-based network observation of Asian dust events of April 1998 in east Asia. *Journal of Geophysical Research: Atmospheres* 106(D16):18345–18359. 00316.
- Nam, Jihyun, Sang-Woo Kim, Rokjin J. Park, Jin-Soo Park, and Sang Seo Park. 2018. Changes in column aerosol optical depth and ground-level particulate matter concentration over East Asia. *Air Quality, Atmosphere & Health* 11(1):49–60. 00000.
- Nishizawa, Tomoaki, Nobuo Sugimoto, Ichiro Matsui, Atsushi Shimizu, Yukari Hara, Uno Itsushi, Kazuaki Yasunaga, Rei Kudo, and Sang-Woo Kim. 2017. Ground-based network observation using Mie–Raman lidars and multi-wavelength Raman lidars and algorithm to retrieve distributions of aerosol components. *Journal of Quantitative Spectroscopy and Radiative Transfer* 188:79–93. 00015.
- Noh, Young M., Young J. Kim, and Detlef Müller. 2008. Seasonal characteristics of lidar ratios measured with a Raman lidar at Gwangju, Korea in spring and autumn. *Atmospheric Environment* 42(9):2208–2224. 00061.
- Panicker, A. S., D. I. Lee, Y. V. Kumkar, D. Kim, M. Maki, and H. Uyeda. 2013. Decadal climatological trends of aerosol optical parameters over three different environments in South Korea. *International Journal of Climatology* 33(8):1909–1916. 00029.
- Peel, M C, B L Finlayson, and T A McMahon. 2007. Updated world map of the Koppen-Geiger climate classification. *Hydrol. Earth Syst. Sci.* 12. 00000.
- Peng, Jian, Sha Chen, Huiling Lü, Yanxu Liu, and Jiansheng Wu. 2016. Spatiotemporal patterns of remotely sensed PM_{2.5} concentration in China from 1999 to 2011. *Remote Sensing of Environment* 174:109–121. 00062.
- Piironen, P., and E. W. Eloranta. 1994. Demonstration of a high-spectral-resolution lidar based on an iodine absorption filter. *Optics Letters* 19(3):234–236. 00207.

- Pinnick, R. G., S. G. Jennings, Petr Chýlek, Chris Ham, and W. T. Grandy. 1983. Backscatter and extinction in water clouds. *Journal of Geophysical Research: Oceans* 88(C11):6787–6796.
- Qin, Wenmin, Ying Liu, Lunche Wang, Aiwen Lin, Xiangao Xia, Huizheng Che, Muhammad Bilal, Ming Zhang, Wenmin Qin, Ying Liu, Lunche Wang, Aiwen Lin, Xiangao Xia, Huizheng Che, Muhammad Bilal, and Ming Zhang. 2018. Characteristic and Driving Factors of Aerosol Optical Depth over Mainland China during 1980–2017. *Remote Sensing* 10(7):1064. 00000.
- Qu, Wenjun, Jun Wang, Xiaoye Zhang, Lifang Sheng, and Wencai Wang. 2016. Opposite seasonality of the aerosol optical depth and the surface particulate matter concentration over the north China Plain. *Atmospheric Environment* 127: 90–99. 00011.
- Quan, Jiannong, Yang Gao, Qiang Zhang, Xuexi Tie, Junji Cao, Suqin Han, Junwang Meng, Pengfei Chen, and Delong Zhao. 2013. Evolution of planetary boundary layer under different weather conditions, and its impact on aerosol concentrations. *Particuology* 11(1):34–40. 00118.
- Razenkov, Ilya. 2010. Characterization of a Geiger-mode avalanche photodiode detector for high spectral resolution lidar. PhD Thesis, University of Wisconsin—Madison. 00006.
- Sakai, Tetsu, Tomohiro Nagai, Yuji Zaizen, and Yuzo Mano. 2010. Backscattering linear depolarization ratio measurements of mineral, sea-salt, and ammonium sulfate particles simulated in a laboratory chamber. *Applied Optics* 49(23):4441–4449. 00052.
- Seinfeld, John H., and Spyros N. Pandis. 1998. *Atmospheric Chemistry and Physics: From Air Pollution to Climate Change*. John Wiley & Sons. Google-Books-ID: n_RmCgAAQBAJ.
- Sharma, Atul Prakash, Ki-Hyun Kim, Ji-won Ahn, Zang-Ho Shon, Jong-Ryeul Sohn, Jin-Hong Lee, Chang-Jin Ma, and Richard J. C. Brown. 2014. Ambient

particulate matter (PM₁₀) concentrations in major urban areas of Korea during 1996–2010. *Atmospheric Pollution Research* 5(1):161–169. 00020.

Shi, Y., J. Zhang, J. S. Reid, B. Liu, and E. J. Hyer. 2014. Critical evaluation of cloud contamination in the MISR aerosol products using MODIS cloud mask products. *Atmos. Meas. Tech.* 7(6):1791–1801. 00000.

Shimizu, Atsushi, Nobuo Sugimoto, Ichiro Matsui, Kimio Arao, Itsushi Uno, Toshiyuki Murayama, Naoki Kagawa, Kazuma Aoki, Akihiro Uchiyama, and Akihiro Yamazaki. 2004. Continuous observations of Asian dust and other aerosols by polarization lidars in China and Japan during ACE-Asia. *Journal of Geophysical Research: Atmospheres* 109(D19). 00394.

da Silva, Arlindo Colarco. 2011. An Overview of the GEOS-5 Aerosol Reanalysis. In *An Overview of the GEOS-5 Aerosol Reanalysis*. San Francisco, CA, United States. 00004.

Su, Wenying, Gregory L. Schuster, Norman G. Loeb, Raymond R. Rogers, Richard A. Ferrare, Chris A. Hostetler, Johnathan W. Hair, and Michael D. Obland. 2008. Aerosol and cloud interaction observed from high spectral resolution lidar data. *Journal of Geophysical Research: Atmospheres* 113(D24). 00071.

Sugimoto, Nobuo, Itsushi Uno, Masataka Nishikawa, Atsushi Shimizu, Ichiro Matsui, Xuhui Dong, Yan Chen, and Hao Quan. 2003. Record heavy Asian dust in Beijing in 2002: Observations and model analysis of recent events. *Geophysical Research Letters* 30(12). 00210.

Takeuchi, Nobuo, and Tatsuru Sato. 1987. Geometrical Form Factor of the Lidar with a Narrow-Band Interference Filter. *The Review of Laser Engineering* 15(5): 296–306. 00005.

Tesche, M., A. Ansmann, D. Müller, D. Althausen, R. Engelmann, V. Freudenthaler, and S. Groß. 2009. Vertically resolved separation of dust and smoke over Cape

Verde using multiwavelength Raman and polarization lidars during Saharan Mineral Dust Experiment 2008. *Journal of Geophysical Research: Atmospheres* 114(D13). 00178.

Toth, Travis D., Jianglong Zhang, Jeffrey S. Reid, and Mark A. Vaughan. 2019. A bulk-mass-modeling-based method for retrieving particulate matter pollution using CALIOP observations. *Atmospheric Measurement Techniques* 12(3):1739–1754. 00000.

UNdata. 2019. UNdata. 00064.

Vande Hey, Joshua, Jeremy Coupland, Ming Hui Foo, James Richards, and Andrew Sandford. 2011. Determination of overlap in lidar systems. *Applied Optics* 50(30): 5791. 00015.

Várnai, Tamás, and Alexander Marshak. 2009. MODIS observations of enhanced clear sky reflectance near clouds. *Geophysical Research Letters* 36(6). 00107.

WHO, World Health Organization and others. 2016. Ambient air pollution: A global assessment of exposure and burden of disease. *World Health Organization*. 00344.

Xia, Xiangao, Tom F. Eck, Brent N. Holben, Goloub Phillippe, and Hongbin Chen. 2008. Analysis of the weekly cycle of aerosol optical depth using AERONET and MODIS data. *Journal of Geophysical Research: Atmospheres* 113(D14). 00049.

Yamaji, Kazuyo, Toshimasa Ohara, Itsushi Uno, Hiroshi Tanimoto, Jun-ichi Kurokawa, and Hajime Akimoto. 2006. Analysis of the seasonal variation of ozone in the boundary layer in East Asia using the Community Multi-scale Air Quality model: What controls surface ozone levels over Japan? *Atmospheric Environment* 40(10):1856–1868.

Yu, Hongbin, Mian Chin, David M. Winker, Ali H. Omar, Zhaoyan Liu, Chieko Kittaka, and Thomas Diehl. 2010. Global view of aerosol vertical distributions

from CALIPSO lidar measurements and GOCART simulations: Regional and seasonal variations. *Journal of Geophysical Research: Atmospheres* 115(D4). 00140.

Zhang, Qiang, XinCheng Ma, Xuexi Tie, Mengyu Huang, and Chunsheng Zhao. 2009. Vertical distributions of aerosols under different weather conditions: Analysis of in-situ aircraft measurements in Beijing, China. *Atmospheric Environment* 43(34):5526–5535.

Zhang, Yunjiang, Olivier Favez, Francesco Canonaco, Dantong Liu, Griša Močnik, Tanguy Amodeo, Jean Sciare, André S. H. Prévôt, Valérie Gros, and Alexandre Albinet. 2018. Evidence of major secondary organic aerosol contribution to lensing effect black carbon absorption enhancement. *npj Climate and Atmospheric Science* 1(1):47. 00000.